Applied Mathematical Modelling 40 (2016) 6934–6955

Contents lists available at ScienceDirect

Applied Mathematical Modelling

journal homepage: www.elsevier.com/locate/apm

A central scheme for advecting scalars by velocity fields obtained from Finite Volume multiphase incompressible solvers

Santiago Márquez Damián [a,*], Norberto M. Nigro [a], Gustavo C. Buscaglia [b]

[a] Centro de Investigación de Métodos Computacionales (CIMEC), UNL/CONICET, Colectora Ruta Nac. 168/Paraje El Pozo, 3000 Santa Fe, Argentina

[b] Instituto de Ciências Matemáticas e de Computação (ICMC), Av. do Trabalhador Sãocarlense 400, Centro, CEP 13560-970 São Carlos, SP, Brasil

ARTICLE INFO

Article history:
Received 22 December 2014
Revised 31 December 2015
Accepted 18 February 2016
Available online 3 March 2016

Keywords:
Central schemes
Cell centered Finite Volume Method
Incompressible flow
PISO scheme
Multiphase flows
Mixture model

ABSTRACT

This paper presents an extension of the central scheme of Kurganov and Tadmor (2000) to work with solvers based on conservative face fluxes, which are usual in the solution of incompressible flows by the Finite Volume Method. The proposed scheme retains the desirable properties of simplicity, low numerical viscosity and multidimensionality, and it works on general non-staggered polyhedral meshes. It is applied within a mixture multiphase solver to discretize the mass conservation equation of one of the phases. A series of cases are solved which show that the proposed extension is significantly more robust and monotonicity-preserving than the straightforward application of the Kurganov–Tadmor scheme.

1. Introduction

Central schemes have attracted much attention due to their simplicity and effectiveness to solve hyperbolic partial differential equations. The principal advantage is that no Riemann problems have to be solved either exactly or using Godunov methods which require the analysis of upwind directions on the Riemann fan.

Starting from the seminal work of Lax [1] with the celebrated Lax–Friedrichs (LxF) scheme, central schemes have been improved in accuracy in space and time discretization. The first extension was due to Nessyahu and Tadmor (NT) [2] who obtained a second order generalization of the LxF scheme, decreasing the numerical viscosity from $\mathcal{O}(\Delta x^2/\Delta t)$ to $\mathcal{O}(\Delta x^4/\Delta t)$. The key concept was to replace the piecewise constant reconstruction of the solution by a piecewise linear representation with limited slopes [3]. This scheme has two main drawbacks: (1) it requires the use of staggered meshes and (2) the numerical viscosity increases for small time steps. Kurganov and Tadmor (KT) [4] removed these requirements and presented a second order central scheme with numerical viscosity of $\mathcal{O}(\Delta x^4)$ which accepts a semi-discrete formulation in a non-staggered grid.

* Corresponding author. Tel.: +5493424511594x7032.
E-mail address: santiagomarquezd@gmail.com (S. Márquez Damián).
URL: http://www.cimec.org.ar (S. Márquez Damián), http://www.cimec.org.ar (N.M. Nigro), http://www.icmc.usp.br/ (G.C. Buscaglia)

http://dx.doi.org/10.1016/j.apm.2016.02.034
S0307-904X(16)30108-1/

A remarkable characteristic of the KT is the direct extension to multidimensions, this topic was addressed by Kurganov and Tadmor in the presentation of the scheme. Thus, it is extended from the one dimensional case to more dimensions using the so-called *dimension-by-dimension* formulation. It implies the splitting of the original hyperbolic equation defining fluxes by the Cartesian directions. Truly multidimensional extensions were presented later, for the case of structured and triangular two dimensional meshes, Kurganov and Petrova [5,6] achieved such extensions using polynomial interpolants. Even though more improvements were done following the same line [7,8] none of them is capable to manage truly polyhedral collocated meshes. In this context, Greenshields et al. [9] made a valuable contribution treating arbitrary polyhedral meshes using a *face-by-face* reconstruction, recalling the original concepts of one dimensional central schemes of Kurganov and Tadmor but applied in the face normal direction.

Application of central schemes to single phase flows started considering the compressible case, in which the whole equation system is hyperbolic. Extension to multiphase flows also considered hyperbolic problems, such as those obtained by linking the density of each phase to the local pressure [10–13].

Central schemes were adapted for single phase incompressible flows by Kupferman [14], and have also been applied to viscoelastic liquids [15–18]. These contributions addressed particularly the solution of the momentum equation, the incidence of wave directions and capturing was not discussed. The schemes used were derived from the NT method in staggered structured meshes and were implemented by the Finite Difference Method. The application of KT schemes was later extended to multiphase porous media flow by Abreu et al. [19], Furtado et al. [3], and Pereira and Rahunanthan [20] with a special treatment of the coupling between the incompressibility restriction and the central advection scheme used to solve the Buckley–Leverett equation for the concentration. Their method was introduced considering Cartesian rectangular meshes with Raviart–Thomas finite elements for the computation of pressure and velocity. A key concept in the success of the method of Abreu et al. is the use of divergence-free fluxes in the advection of the concentration variables.

In this article an unstructured version of the method of Abreu et al. is introduced, which is capable to solve hyperbolic equations with a conservative flux given at faces and obtained in a pressure–velocity coupling loop (PISO) [21,22] and a nonlinear flux calculated by an explicit flux function (KTcFlux, Kurganov and Tadmor with conservative flux). The computation of the concentration fluxes uses the divergence-free velocities at faces obtained from the PISO algorithm together with the face-by-face reconstruction of concentration values proposed by Greenshields et al. The resulting scheme is an efficient cell-centered finite volume method for arbitrary meshes, that is locally and globally conservative and allows for capturing the shocks, rarefactions and compound waves which are usual in the solution of the multiphase systems [23].

The manuscript is organized as follows: the Section 1 represents the introduction. Next, in Section 2, some basic concepts of KT schemes are revisited and the KTcFlux is derived in semi-discrete form and extended to multidimensions. Section 3 presents an application of the present scheme to a multiphase mixture model. The obtained scheme is then applied to three examples which are presented in Section 4 and require the correct treatment of different kind of traveling waves. Finally, Section 5 presents the conclusions.

2. A Riemann-free solver with centered flux

2.1. The model hyperbolic equation

The application of central schemes is related to the non-linear hyperbolic model equation:

$$\frac{\partial}{\partial t}\vec{u}(\vec{x},t)+\vec{\nabla}\cdot\overline{\overline{\mathcal{F}}}(\vec{u}(\vec{x},t))=0, \tag{1}$$

where $\vec{u}$ is a vector of conserved quantities in a multidimensional space and $\overline{\overline{\mathcal{F}}}(\vec{u}(\vec{x},t))$ is a non-linear tensorial convection flux of the conserved quantities. These equations are commonly present in the description of problems of transport phenomena [24]. The discretization of Eq. (1) by the cell centered Finite Volume Method [22,25] using volume integrals and the Gauss theorem for the flux term leads to:

$$\int_{\Omega_j}\frac{\partial}{\partial t}\vec{u}(\vec{x},t)\,d\Omega+\int_{\Gamma_j}\overline{\overline{\mathcal{F}}}(\vec{u}(\vec{x},t))\cdot d\vec{\Gamma}\cong\frac{\partial}{\partial t}\bar{\vec{u}}_j V_\Omega+\sum_f\overline{\overline{\mathcal{F}}}(\bar{\vec{u}})_f\cdot\vec{S}_f=\frac{\partial}{\partial t}\bar{\vec{u}}_j V_{\Omega_j}+\sum_f\vec{\mathrm{F}}_f=0, \tag{2}$$

where Ω_j is the volumetric domain of a given faceted finite volume j of the discretization, Γ_j is its boundary, V_{Ω_j} is the volume and $\bar{\vec{u}}_j$ and $(\bar{\vec{u}})_f$ the average values of $\vec{u}$ at cell centers and faces. In addition, f represents the index for each face of Ω_j, $\vec{S}_f$ the corresponding face area vector and $\vec{\mathrm{F}}_f=\overline{\overline{\mathcal{F}}}\cdot\vec{S}_f$ the total face flux.

2.2. One dimensional semi-discrete form

The derivation of the one dimensional semi-discrete form of the present scheme starts from the original Kurganov and Tadmor scheme, then it is worthy to recall some definitions (see Fig. 1):

- u: is the continuous function being integrated in time and space (scalar case of $\vec{u}$);
- $\bar{u}$: is a sliding average of u obtained by Eq. (3)
- $\tilde{u}$: is a piecewise linear approximation of u defined in Eq. (4).

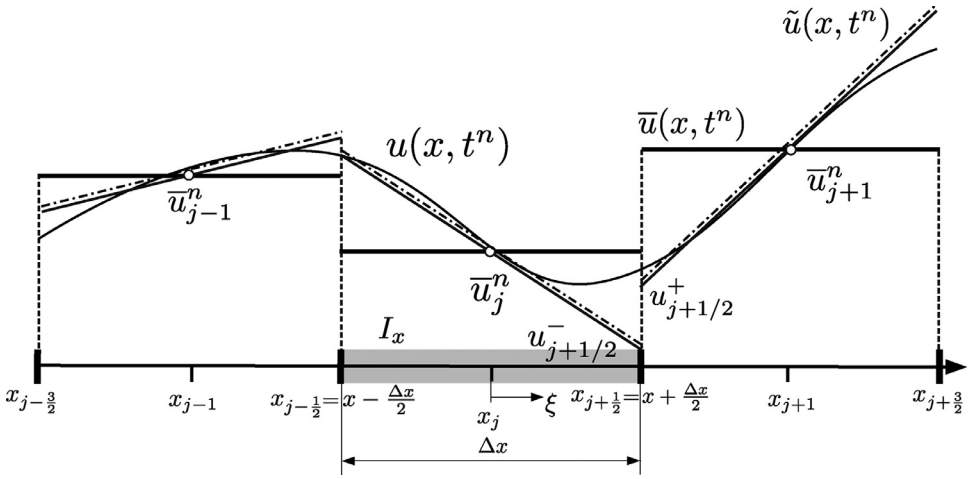

Fig. 1. Original continuous function u (continuous thin line), $\overline{u}$ piecewise constant approximation (continuous thick line), $\tilde{u}$ piecewise linear approximation (dash dotted line). The discretization cell is hatched in gray.

$$\overline{u}(x,t^n)=\frac{1}{|I_x|}\int_{I_x}u(\xi,t)\,d\xi,\quad I_x=\left\{\xi:|\xi-x|\leqslant\frac{\Delta x}{2}\right\},\tag{3}$$

$$\tilde{u}(x,t^n)=\sum_j\left[\overline{u}^n_j+(u_x)^n_j(x-x_j)\right]\mathbf{1}_{[x_{j-1/2},x_{j+1/2}]},\quad x_{j\pm1/2}=x_j+\frac{\Delta x}{2},\tag{4}$$

where $\mathbf{1}_{[x_{j-1/2},x_{j+1/2}]}$ is the indicator function which has a value of 1 within the interval given in the sub-index and zero otherwise. The calculation of the piecewise linear approximation requires the values of $(u_x)^n_j$ which are approximations to the exact derivatives $u_x(x_j,t^n)$ and are computed from the cell averages $\overline{u}^n_j$. The computation of such approximate derivatives relies on TVD methods [26]. In addition the values of $\overline{u}^n_j$ are approximated as $\overline{u}^n_j\cong\overline{u}(x_j,t^n)=\int_{I_x}u(\xi,t^n)d\xi/\Delta x$.

Finally, this scheme relies on a stabilization for the advective terms based on the *local* speeds of wave propagation, which for the most practical applications can be defined as:

$$a^n_{j+1/2}:=\max\left\{\rho\left(\frac{\partial\mathcal{F}}{\partial u}(u^-_{j+1/2})\right),\rho\left(\frac{\partial\mathcal{F}}{\partial u}(u^+_{j+1/2})\right)\right\},\tag{5}$$

where ρ is the spectral radius of the $\frac{\partial\mathcal{F}}{\partial u}$ matrix at each side of a face and $u^-_{j+1/2}$, $u^+_{j+1/2}$ are the values of $\tilde{u}$ at both sides of the $x_{j+\frac{1}{2}}$ cell interface. As is explained in the work of Kurganov and Tadmor, the values of the continuous function being integrated, u, differ in a negligible second order term with cell averages, $\overline{u}$, then the overbar is usually dropped in the presentation of the scheme.

The derivation of the present scheme starts from the *Kurganov and Tadmor semi-discrete* formulation (see Appendix A):

$$\begin{aligned}\frac{d}{dt}u_j(t)=&-\frac{\left[\mathcal{F}\left(u^+_{j+1/2}(t)\right)+\mathcal{F}\left(u^-_{j+1/2}(t)\right)\right]-\left[\mathcal{F}\left(u^+_{j-1/2}(t)\right)+\mathcal{F}\left(u^-_{j-1/2}(t)\right)\right]}{2\,\Delta x}\\&+\frac{1}{2\,\Delta x}\left\{a_{j+1/2}(t)\left[u^+_{j+1/2}(t)-u^-_{j+1/2}(t)\right]-a_{j-1/2}(t)\left[u^+_{j-1/2}(t)-u^-_{j-1/2}(t)\right]\right\},\end{aligned}\tag{6}$$

where the intermediate values are defined as:

$$u^+_{j+1/2}(t):=u_{j+1}(t)-\frac{\Delta x}{2}(u_x)_{j+1}(t)\quad u^-_{j+1/2}(t):=u_j(t)+\frac{\Delta x}{2}(u_x)_j(t),\tag{7}$$

Finally, this scheme admits the conservative form:

$$\frac{d}{dt}u_j(t)=-\frac{H_{j+1/2}(t)-H_{j-1/2}(t)}{\Delta x},\tag{8}$$

with a numerical flux given by:

$$H_{j+1/2}(t):=\frac{\mathcal{F}\left(u^+_{j+1/2}(t)\right)+\mathcal{F}\left(u^-_{j+1/2}(t)\right)}{2}-\frac{a_{j+1/2}(t)}{2}\left[\left(u^+_{j+1/2}(t)-u^-_{j+1/2}(t)\right)\right].\tag{9}$$

Here it is important to remark that the Kurganov and Tadmor scheme has second order accuracy, which is ensured by the piecewise linear reconstruction used in its construction [27]. The numerical viscosity is of order $\sim(\Delta x)^3(a(u)u_{xxx})_x/8$ and is independent of Δt, setting an important difference with respect to LxF and NT schemes.

Now it is possible to propose a scheme for a flux having a nonlinear part and an explicitly written linear advection term, as is presented in Eq. (10):

$$\mathcal{F}(u(x,t)) = \mathcal{F}^{\mathrm{R}}(u(x,t)) + v(x,t)\,u(x,t). \tag{10}$$

Here, $\mathcal{F}(u,t)^{\mathrm{R}}$ is an autonomous nonlinear flux and the linear advection term is formed by a given velocity v which satisfies the incompressibility restriction $\partial v(x,t)/\partial x = 0$ or in the general multidimensional case $\vec{\nabla}\cdot\vec{v}(\vec{x},t) = 0$. This velocity is obtained by a pressure–velocity coupling procedure as a part of an incompressible flow solver. Thus, since v obeys the incompressibility restriction it is single valued at faces which leads to propose the following centered scheme (KTcFlux):

$$\begin{aligned}\frac{d}{dt}u_j(t) = &-\frac{\left(\mathcal{F}^{\mathrm{R}}(u^+_{j+1/2}) + \mathcal{F}^{\mathrm{R}}(u^-_{j+1/2,})\right) - \left(\mathcal{F}^{\mathrm{R}}(u^+_{j-1/2}) + \mathcal{F}^{\mathrm{R}}(u^-_{j-1/2})\right)}{2\Delta x}\\ &-\frac{\left(v_{j+1/2}u^+_{j+1/2} + v_{j+1/2}u^-_{j+1/2}\right) - \left(v_{j-1/2}u^+_{j-1/2} + v_{j-1/2}u^-_{j-1/2}\right)}{2\Delta x}\\ &+\frac{1}{2\Delta x}\left\{a_{j+1/2}(t)[u^+_{j+1/2}(t) - u^-_{j+1/2}(t)] - a_{j-1/2}(t)[u^+_{j-1/2}(t) - u^-_{j-1/2}(t)]\right\},\end{aligned} \tag{11}$$

where terms in the first line of the right hand side correspond to the nonlinear term of the original hyperbolic equation, the terms in the second line are calculated using the velocity v obtained in the pressure–velocity coupling and the terms in the last line correspond to the stabilization. The obtained scheme admits the conservative form:

$$\frac{d}{dt}u_j(t) = -\frac{C_{j+1/2}(t) - C_{j-1/2}(t)}{\Delta x}, \tag{12}$$

where $C_{j+1/2}(t)$ is a numerical flux defined as:

$$C_{j+1/2(t)} = \frac{\mathcal{F}^{\mathrm{R}}(u^+_{j+1/2}) + \mathcal{F}^{\mathrm{R}}(u^-_{j+1/2,})}{2} + \frac{v_{j+1/2}(u^+_{j+1/2} + u^-_{j+1/2})}{2} - \frac{a_{j+1/2}(t)}{2}[u^+_{j+1/2}(t) - u^-_{j+1/2}(t)]. \tag{13}$$

2.3. Multidimensional and unstructured extension

A generalization of the proposed Riemann-free solver with centered flux to multidimensions requires to be able to manage polyhedral meshes. The implementation for structured and triangular meshes by Kurganov and Petrova [5,6] sets a reference for truly multidimensional approaches. Extensions of these schemes in case of three dimensional meshes were presented later [7,8,28] applied to tetrahedral elements, nevertheless no complete polyhedral extension is available to the present day. This work follows the contribution of Greenshields et al. [9], which allows for a native treatment of unstructured meshes by the so-called *face-by-face* reconstruction, applying the one dimensional scheme through the face normal directions. In this context, the novelty is the addition of the terms corresponding to the linear part of the flux keeping the conservation properties of the original pressure–velocity coupling. Therefore, recalling the discretization of the model hyperbolic equation [Eq. (2)] and writing it for a scalar conserved quantity, it reads:

$$\frac{\partial}{\partial t}u(x,t)\,V_\Omega + \sum_f \vec{\mathcal{F}}(u(x,t))_f\cdot\vec{S}_f = \frac{\partial}{\partial t}u(x,t)\,V_\Omega + \sum_f \mathrm{F}_f = 0,$$

where $\vec{\mathcal{F}}(u(x,t))_f$ is the convective flux vector calculated from the u face values, reconstructed by some TVD method. As were presented, the KT methods are based in face reconstructed values at both sides of a face and the information given by the eigenvalues or *local speeds*. In a polyhedral mesh this reconstruction is done face-by-face in a fully multi-dimensional framework. The interpolation procedure is split in two directions according to the face area vector $\vec{S}_f$; the $(+)$ direction coincides with $\vec{S}_f$ and the opposite for the case of $(-)$, as is shown in Fig. 2. Then, the flux balance term in KT methods can be written as:

$$\sum_f \mathrm{F}_f = \sum_f\left[\frac{1}{2}\mathrm{F}_{f+} + \frac{1}{2}\mathrm{F}_{f-} - \frac{1}{2}\,a_f(u_{f+} - u_{f-})\right], \tag{14}$$

where a_f are the local speeds at faces in the sense of KT [see Eq. (5)]. These local speeds are calculated as face fluxes in a multidimensional framework as:

$$a_f = \max\left\{\rho\left(\frac{\partial\vec{\mathcal{F}}}{\partial u}\cdot\vec{S}_f\right)_{f+}, \rho\left(\frac{\partial\vec{\mathcal{F}}}{\partial u}\cdot\vec{S}_f\right)_{f-}\right\}, \tag{15}$$

Finally, it is necessary to define the flux $\mathrm{F}_f = \mathrm{F}^{\mathrm{R}}_f + \mathrm{F}^{\mathrm{c}}_f$ in terms of the reconstructed flux $\mathrm{F}^{\mathrm{R}}_f = \vec{\mathcal{F}}^{\mathrm{R}}_f\cdot\vec{S}_f$ and the centered flux given at faces by the pressure–velocity coupling (PISO), $F^c = \vec{v}_f\cdot\vec{S}_f$, with $\mathrm{F}^{\mathrm{c}}_f = F^c\,u_f = \vec{v}_f\cdot\vec{S}_f\,u_f$ as in Eq. (10), which leads to:

$$\sum_f \mathrm{F}_f = \sum_f\left[\frac{1}{2}\left(\mathrm{F}^{\mathrm{R}}_{f+} + F^c\,u_{f+}\right) + \frac{1}{2}\left(\mathrm{F}^{\mathrm{R}}_{f-} + F^c\,u_{f-}\right) - \frac{1}{2}\,a_f(u_{f+} - u_{f-})\right]$$

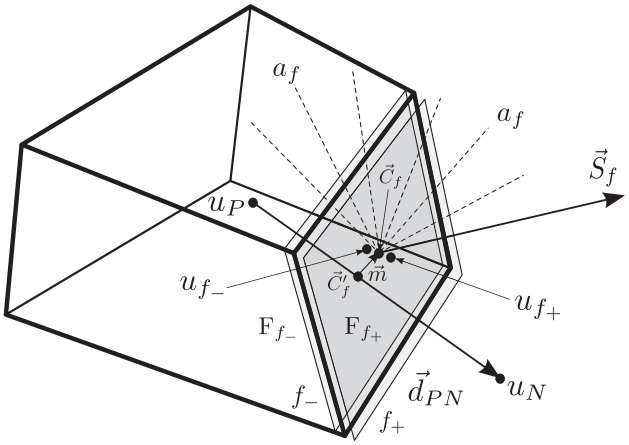

Fig. 2. Detail of a single mesh cell.

$$= \sum_f \left[\frac{1}{2}\left(\mathrm{F}^{\mathrm{R}}_{f+} + \mathrm{F}^{\mathrm{R}}_{f-}\right) + \frac{1}{2} F^c \left(u_{f+} + u_{f-}\right) - \frac{1}{2} a_f \left(u_{f+} - u_{f-}\right) \right]. \tag{16}$$

The evaluation of u values at both sides of each face, u_{f+} and u_{f-} requires the implementation of TVD reconstruction methods in a polyhedral framework. This task is achieved using a generalization of the Sweby functions, ψ, by Sweby [29], and Darwish and Moukalled [30]:

$$u_{f+} = u_N + \lambda(r_{f+})\,(u_P - u_N) \quad u_{f-} = u_P + \lambda(r_{f-})\,(u_N - u_P), \tag{17}$$

where $\lambda(r_f)$ is a blending factor related to the Sweby function [22,31], ψ, in the following way:

$$\lambda(r_f) = [1 - \psi(r_f)]\, f_{x,\mathrm{UD}} + \psi(r_f)\, f_{x,\mathrm{CD}}, \tag{18}$$

and $f_{x,\mathrm{UD}} = 1$ and $f_{x,\mathrm{CD}} = \overline{fN}/\overline{PN}$ are the standard interpolation factors for upwind and central differencing. The user selected function, ψ, sets the kind of TVD reconstruction at faces. The Sweby function requires to calculate the r factor,

$$r_{f+} = \frac{2\vec{\nabla} u_P \cdot \vec{d}_{PN}}{u_N - u_P} - 1 \quad r_{f-} = \frac{2\vec{\nabla} u_N \cdot (-\vec{d}_{PN})}{u_P - u_N} - 1, \tag{19}$$

where $\vec{\nabla} u_{P,N}$ is the gradient of u at cells P, N and $\vec{d}_{PN} = \vec{x}_N - \vec{x}_P$.

The discretization of the divergence operator in the FVM suffers the influence of the skewness errors, as a product of the face interpolation, Eq. (17), from cell-centered values. This error may lead second-order accurate scheme to first order accuracy. A solution is to apply an explicit correction based on the gradient to approximate the face values, $u_{f+} = u'_{f+} + \vec{\nabla} u_f \cdot \vec{m}$. This kind of correction is available in OpenFOAM® but is known to be potentially unbounded [32]. Recently Denner and van Wachem [33] proposed a bounded skewness correction with application to TVD schemes in unstructured meshes. It is based on the modification of the original Sweby functions to include the skewness correction and to lie within the monotonicity region in the TVD diagram at the same time. Since this is scheme is also formally first order accurate it is preferred to keep the simplicity of the original TVD schemes provided the use of low skewness meshes. Finally, the calculation of the r factor in Eq. (19) requires low mesh gradings to avoid additional accuracy losses [22].

2.4. Determination of the centered flux at faces

With respect to the values of $\vec{v}_f$, it deserves a discussion. The pressure–velocity coupling methods such as PISO [21,22] give at the end of the coupling loop the values of $\vec{v}$ at cell-centers and also in faces in the form of a flux. Thus, there are at least two possible forms to evaluate the linear advection term of the KTcFlux scheme:

1. Following the guidelines from KT schemes, i.e. evaluating v_f from cell-centered velocities (*Interpolated velocities method*);
2. taking advantage of the pre-computed face-fluxes given by the PISO loop (*Face fluxes method*).

The first proposal implies having $\vec{v}_f = f(\vec{v}_P, \vec{v}_N)$, in this case a linear interpolation based on face to cell-center distances is used. For the second case the fluxes obtained by the PISO loop are used:

$$\mathrm{F}^{\mathrm{c}}_f = F^c_{\mathrm{PISO}}\, u_f. \tag{20}$$

Using this expression requires to modify the calculation of the local speeds to include the pre-computed fluxes. Thus, recalling the global flux definition given by Eq. (10) and writing it for the vector case:

$$\vec{\mathcal{F}}(u(x,t)) = \vec{\mathcal{F}}^{\mathrm{R}}(u(x,t)) + \vec{v}(x,t)\, u(x,t), \tag{21}$$

and the definition of the local speeds for the multidimensional case, given by Eq. (15), it is possible to obtain the new expression for the local speeds:

$$a_f = \max\left\{ \rho\left(\frac{\partial \vec{\mathcal{F}}^{\mathrm{R}}}{\partial u} \cdot \vec{S}_f + F^c_{\mathrm{PISO}} \right)_{f+}, \rho\left(\frac{\partial \vec{\mathcal{F}}^{\mathrm{R}}}{\partial u} \cdot \vec{S}_f + F^c_{\mathrm{PISO}} \right)_{f-} \right\}. \tag{22}$$

The effects of these formulations will be presented in Section 4.1.

3. Application to a multiphase solver

The solution of non-linear hyperbolic equations along with the momentum equations with incompressibility restriction is common in problems of porous media (Buckley–Leverett equation) [3,19,20], and in monodisperse and polydisperse multifluid flows (via the Euler–Euler multifluid model or Mixture Models) [34–38]. Here the KTcFlux method will applied to a multiphase solver based on the Algebraic Slip Mixture Model (ASMM) [23,39]. In this model both of the phases are treated as a mixture that exhibits mean properties for density and viscosity, as in shown in Eq. (23)*a–c*. It is composed by the incompressibility restriction (*a*), the momentum equation for the mixture (*b*), and the phase distribution conservation equation (*c*), written either in terms or the dispersed phase, α_p or the continuous one, α_q as is done in this work,

$$\begin{cases} \vec{\nabla} \cdot \vec{v}_v = 0 & \text{(a)} \\ \dfrac{\partial}{\partial t}(\rho_m \vec{v}_m) + \vec{\nabla} \cdot (\rho_m \vec{v}_m \otimes \vec{v}_m) = -\vec{\nabla} p + \vec{\nabla} \cdot \left[\mu_m \left(\vec{\nabla} \vec{v}_m + \vec{\nabla} \vec{v}_m^{\mathrm{T}} \right) \right] + \rho_m \vec{g} & \text{(b)} \\ \dfrac{\partial \alpha_q}{\partial t} + \vec{\nabla} \cdot (\alpha_q \vec{v}_v) + \vec{\nabla} \cdot [\alpha_q (1 - \alpha_q) \vec{v}_{qp}] = 0 & \text{(c)} \end{cases} \tag{23}$$

where the subindex p indicates the dispersed phase, q the continuous phase, α_p and α_q their respective phase fractions (which obey the closure law $\alpha_p + \alpha_q = 1$), $\rho_m = \alpha_p \rho_p + \alpha_q \rho_q$ is the mixture density; $\vec{v}_m = \alpha_p \rho_p \vec{v}_p / \rho_m + \alpha_q \rho_q \vec{v}_q / \rho_m$ is the center-of-mass velocity, which is calculated from the phase velocities $\vec{v}_k$ and the densities ρ_k; p is the pressure, which is common for all the phases; $\mu_m = f(\alpha_p, \mu_p, \mu_q)$ is the dynamic viscosity of the mixture; $\vec{g}$ is the gravitational acceleration; $\vec{v}_v = \alpha_p \vec{v}_p + \alpha_q \vec{v}_q$ is the center-of-volume velocity and $\vec{v}_{qp} = \vec{v}_q - \vec{v}_p$ is the relative velocity of the continuous phase with respect to the dispersed one.

Because the momentum equations for all the phases are not solved, additional algebraic relationships for each phase velocity with respect to the mixture velocity are needed, they are given in the form of relative velocities. The relative velocities are calculated by algebraic expressions related to the physics of the dispersed phase. An example of this kind of laws is given by:

$$\vec{v}_{qp} = \vec{v}_{rc}\, \alpha_q^a = \vec{v}_{rc}\, (1 - \alpha_p)^a = -\vec{v}_{pq}, \tag{24}$$

where $\vec{v}_{rc}$ and a are constants for the model. The $\vec{v}_{rc}$ constant can be interpreted as the velocity of a single bubble or droplet moving in the continuum phase. This expression is flexible and allows to match several other models, for example, the Schiller and Naumann drag law [40] can be fitted by selecting an appropriate value for v_{rc} with $0 \le a \le 1$.

Finally the system of equations for the ASMM presented in Eq. (23) requires a relationship between the center-of-mass velocity $\vec{v}_m$ and center-of-volume velocity $\vec{v}_v$ in order to be closed [41,42]. It is given by following expression:

$$\vec{v}_m = \vec{v}_v + \alpha_q (1 - \alpha_q) \frac{\rho_q - \rho_p}{\rho_m} \vec{v}_{qp}. \tag{25}$$

The solution of the system of equations given in Eq. (23) is then implemented in the cell centered Finite Volume code OpenFOAM® [22,43,44] and relies on conservative fluxes which are obtained by a PISO loop [21]. The solution method is presented in Algorithm 1 and comprises four main steps. In Step 1 the hyperbolic equation for the phases distribution is solved, the flux $F^{c,\,n}$ is taken from the PISO loop in the previous time-step while the nonlinear flux $\mathrm{F}_f^{\mathrm{R},n}$ is computed from the α_q values. Once this step is completed the physical properties are updated (ρ_m, μ_m) and the momentum equation is assembled and solved in Step 2. The final coupling between the center-of-mass velocity and pressure is achieved in Step 3. Finally, in Step 4 the flux for the center-of-volume velocity, $F^{c,\,n}$, is obtained from the flux for $\vec{v}_m$. Here, it is important to remark that the PISO algorithm has an extra term in the pressure equation (Step 3) related to the relative velocities in interphase cells [41,42]. This term appears as consequence of the derivation of a pressure–velocity coupling method based on the incompressibility restriction, $\vec{\nabla} \cdot \vec{v}_v = 0$ in weak form, Eq. (23) *a*, and the relationship between the center-of-mass velocity $\vec{v}_m$ and center-of-volume velocity $\vec{v}_v$. The final step in the algorithm which assembles the face fluxes for the center-of-volume velocity also relies in that relationship. As is shown, the assembling and use of conservative fluxes is a key concept in the whole algorithm and must be taken into account when central schemes are applied.

The solution process presented in Algorithm 1 was originally devised [41] to be used with standard TVD reconstruction at faces, without taking into account the local speeds and their directions. In order to manage this kind of problems the KTcFlux method is applied to Step 1 to solve the conservation equation for the one the phases. Therefore applying the flux calculation method presented in Eqs. (16)–(23) *c* the following expression is obtained:

$$\frac{\alpha_q^{n+1} - \alpha_q^n}{\Delta t} V + \sum_f \left[\frac{1}{2} \left(\mathrm{F}_{f+}^{\mathrm{R},n} + \mathrm{F}_{f-}^{\mathrm{R},n} \right) + \frac{1}{2} F^{c,n} \left(\alpha_{q,f+}^n + \alpha_{q,f-}^n \right) + \frac{1}{2} a_f \left(\alpha_{q,f+}^n - \alpha_{q,f-}^n \right) \right] = 0, \tag{26}$$

Algorithm 1 Pressure based ASMM solver.

1. Solve the phase distribution conservation equation [discretized version of Eq. (23)*c*] using the KTcFlux scheme presented in Eq. (16).

$$\frac{\alpha_q^{n+1}-\alpha_q^n}{\Delta t}V+\sum_f\left[\mathrm{F}_f^{\mathrm{R},n}+F^{c,n}\,\alpha_{q,f}^n\right]=0$$

   where $F^{c,n}=\vec{v}_v\cdot\vec{S}_f$ is a flux of the center-of-volume velocity given at faces which was obtained in the PISO loop of the previous time-step.
2. Solve the momentum predictor [discretized version of Eq. (23)*b*] for $\vec{v}_m$
3. Do the PISO loop in order to correct the velocity obtained in 2) and to find the new pressure and the center-of-mass velocity flux at faces.

$$\sum_f\left[\left(\frac{1}{a_P}\right)_f\left(\vec{\nabla}p^{n+1}\right)_f\right]\cdot\vec{S}_f=\sum_f F_f^{m,n}-\sum_f\left[\alpha_q^{n+1}\left(1-\alpha_q^{n+1}\right)\frac{\rho_q-\rho_p}{\rho_m}\right]_f(\vec{v}_{qp})_f\cdot\vec{S}_f$$

   where $F_f^{m,n}=\vec{v}_m\cdot\vec{S}_f$ is the face flux for the center-of-mass velocity used in the momentum equation.
4. The face flux for the center-of-volume velocity is recovered from the flux

$$F^{c,n+1}=F_f^{m,n+1}-\left[\alpha_q^{n+1}\left(1-\alpha_q^{n+1}\right)\frac{\rho_q-\rho_p}{\rho_m}\right]_f(\vec{v}_{qp})_f\cdot\vec{S}_f$$

where the flux $F^{c,\,n}$ is taken from the PISO loop in the previous time-step and the nonlinear fluxes $\mathrm{F}_{f+}^{\mathrm{R},n}, \mathrm{F}_{f-}^{\mathrm{R},n}$ are computed from the α_q values.

4. Examples

The examples are divided in two groups, the first one is devoted to assess the properties of conservativeness and convergence of the proposed methods and the second one are applications of the KTcFlux to the ASMM multiphase solver. Therefore, in the first group a linear advection problem is solved to evaluate the incidence of the computation of the centered flux at faces, additionally the Burgers equation is solved to introduce some metrics for error evaluation. In the second group, the KTcFlux scheme is applied for the solution of the phase distribution conservation equation, in order to capture the different kind of waves which arise due to its hyperbolicity. The examples consist in problems dominated by buoyant forces in sedimentation and bubble rising phenomena. The cases are presented by increasing complexity in the treatment of the centered flux obtained by the pressure–velocity coupling. In the first problem, the KTcFlux method is used to solve the evolution of dispersed and continuous phases along batch sedimentation. Next, a case with constant centered flux is solved represented by a simplified bubble reactor. Finally, the problem of batch sedimentation is revisited in the case of settling between inclined plates, where the so-called Boycott effect is present. Here, the centered flux can vary in time and space, setting the most general test case for the proposed central scheme.

4.1. Linear advection

In order to test two options for the calculations of velocities at faces, $\vec{v}_f$, the Interpolated velocities method and the Face fluxes method, presented in Section 2.4, are used in an linear advection problem. The problem is set using $\vec{\mathcal{F}}(u(x,t))=\vec{v}(x,t)\,u(x,t)$. The geometry is presented in Fig. 3(a) and corresponds to the flow in a T-junction, with characteristic length, $h=1$[1]. The flow is calculated by an incompressible solver based in the PISO loop with inlets by the lateral boundaries and outlet at the bottom. The velocity field at inlets is given by a parabolic profile with $v_{\max}=1.5$ at $\mathrm{Re}=100$. The domain is meshed with triangles of size ~1/11 [see Fig. 3(b)] and the resulting steady-state velocity field is presented in Fig. 3(a) for the magnitude. Then, the obtained field is used to advect a passive scalar with the KTcFlux scheme using MinMod reconstruction [45], this is set to one on the left inlet and zero on the right inlet and run until $t=5$.

The results for the interpolated velocity method are presented in Fig. 3(c) and (d). In the first picture the resulting u field is shown with the complete scale where is clear that overshoots are found in the solution. These overshoots are better observed in the second figure which highlights the cells having values greater than one. In the case of the face fluxes method, whose results are presented in see Fig. 3(b), the values are always bounded by the extrema set in the initial condition satisfying the monotonicity property of the original differential equation. The differences with the first proposal can be explained from the fact that the incompressibility restriction, $\vec{\nabla}\cdot\vec{v}=0$, is guaranteed by the PISO loop only in weak form ($\sum_f\vec{v}_f\cdot\vec{S}_f=\sum_f F_c=0$) as is usual in Finite Volume Methods. Using the fluxes, F_c, for solving an advection equation

[1] All the magnitudes are expressed in the international system of units.

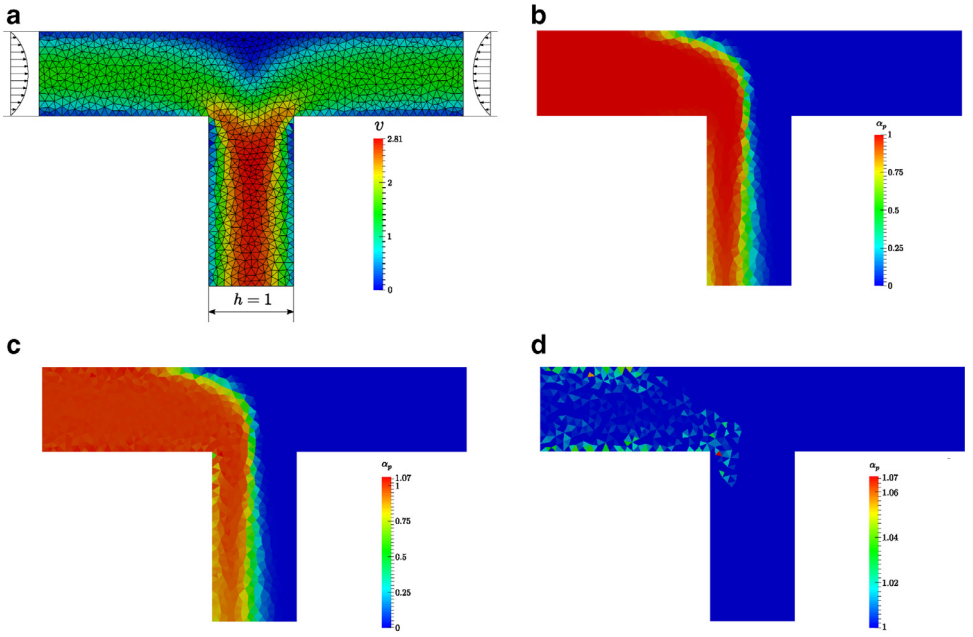

Fig. 3. Linear flux formulations test. (a) Velocity magnitude; (b) solution using given face fluxes; (c) solution by velocity field interpolation; (d) detail of previous figure showing overshoots.

Table 1
Errors for Burgers problem in pre-shock and post-shock cases.

	Pre-shock, $t = 0.5$				Post-shock, $t = 2$			
	L^1 error		*Lip*′ error		L^1 error		*Lip*′ error	
N	KT	Rate	KT	Rate	KT	Rate	KT	Rate
40	5.644E−03	–	1.601E+00	–	2.366E-02	–	9.655E−01	–
80	1.513E−03	1.90	4.141E−01	1.95	1.045E−02	1.18	2.370E−01	2.03
160	4.006E−04	1.92	1.055E−01	1.97	5.427E−03	0.94	6.585E−02	1.85
320	1.055E−04	1.93	2.660E−02	1.99	2.242E−03	1.28	1.743E−02	1.92
640	2.767E−05	1.93	6.664E−03	2.00	1.146E−03	0.97	4.371E−03	2.00
1280	7.191E−06	1.94	1.670E−03	2.00	5.935E−04	0.95	1.071E−03	2.03

leads to a monotonic solution provided that a monotone advection scheme is used (TVD schemes in the present work), as is done in the face fluxes method. Thus, this method will be used hereinafter.

4.2. Burgers equation

This case recalls one of the tests proposed by Kurganov and Tadmor in the presentation of the method. It consists in the solution of the Burgers equation,

$$\frac{\partial \alpha}{\partial t} + \frac{\partial}{\partial z}\left(\frac{\alpha^2}{2}\right) = 0, \tag{27}$$

with smooth initial conditions given by,

$$\alpha(z, 0) = \sin(z) + \frac{1}{2}. \tag{28}$$

This problem develops a shock discontinuity at time $t_c = 1$, then solutions are obtained, for pre-shock time, $t_S = 0.5$ and at post-shock time, $t_D = 2$, as is reported in Fig. 4 for a mesh with 320 elements, using a Runge–Kutta fourth order discretization in time and MinMod [45] scheme for the face reconstruction. The convergence rates are evaluated running in six meshes from 40 to 1280 elements and presented in Table 1. In the pre-shock case the solution exhibits second order convergence in L^1 norm as is expected. Additionally, the convergence rate is computed from the error given in *Lip*′ norm [46], which is a norm designed for solutions with discontinuities and retains the convergence rate for continuous cases as

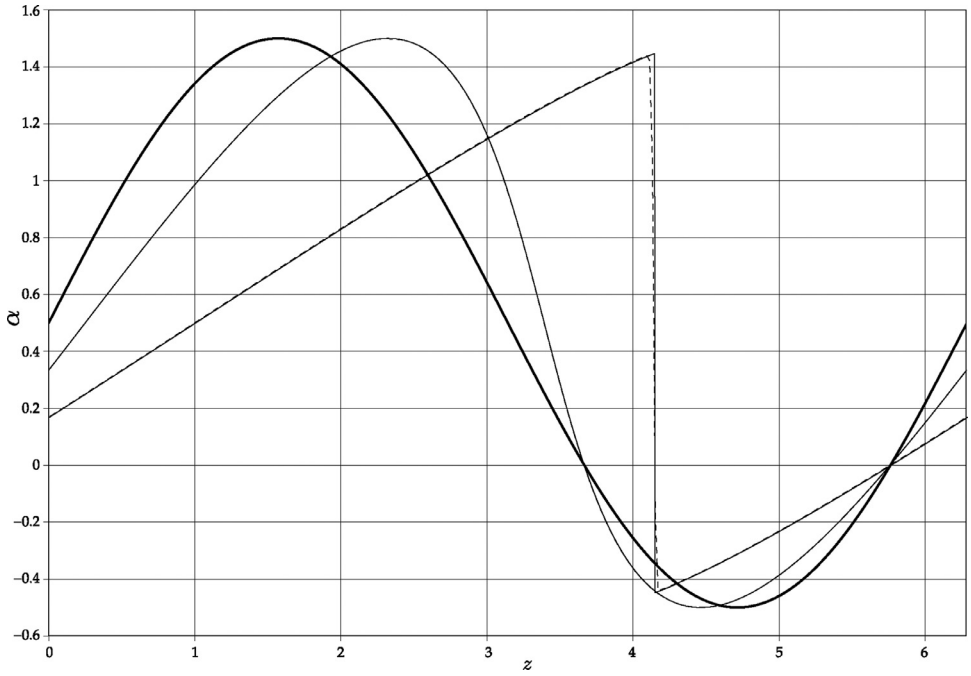

Fig. 4. Initial condition and solutions for Burgers problem. ——— initial condition. Analytical solutions for $t_S = 0.5$ and $t_D = 2$ in continuous thin line, KT solution with MinMod limiter for same times in dashed thin line (solution for $t_S = 0.5$ is coincident with the analytical).

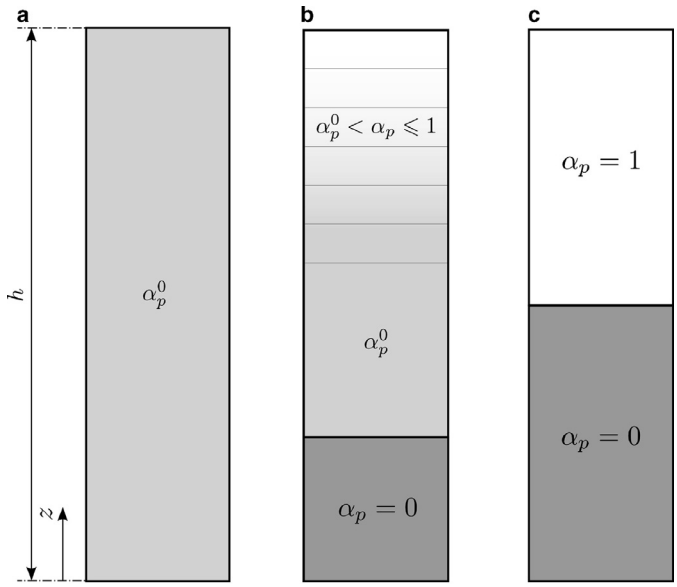

Fig. 5. Batch settling experiment. (a) Initial conditions; (b) settling transitory; (c) steady state.

is observed in the table. In the post-shock case the convergence rate in L^1 norm decreases as is expected for discontinuous solutions [47], but is recovered to second order using the *Lip′* norm, as is presented by Kurganov and Tadmor in their original work.

4.3. Batch settling

The considered case consists in the sedimentation of a mixture of two fluids with different densities within a closed domain, starting from the domain completely filled with the mixture, as it is shown in Fig. 5.

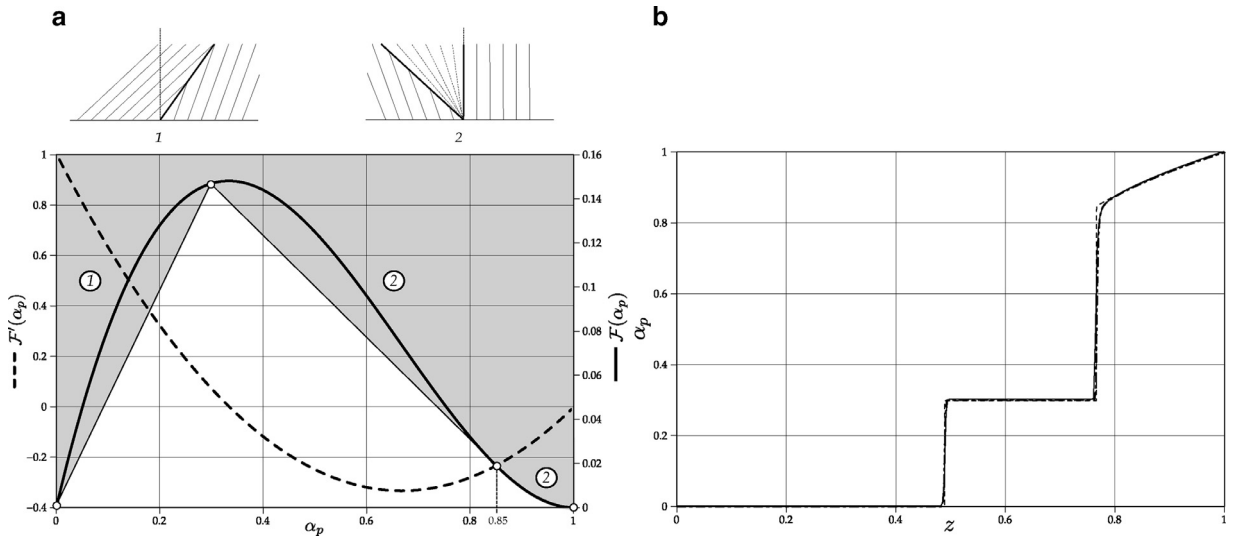

Fig. 6. Batch settling experiment. (*a*) Flux function, $\mathcal{F}(\alpha_p)$, derivative, $\mathcal{F}'(\alpha_p)$ and convex hull plot; (*b*) solution for $t = 1$, ▬▬▬ analytical solution, ▬▬▬ 1D KTcFlux MinMod solution, ▬▬▬ 2D KTcFlux van Leer solution.

Table 2
Errors for batch settling problem.

N	Complete solution				Right going shock			
	L^1 error		*Lip*′ error		L^1 error		*Lip*′ error	
	KT	Rate	KT	Rate	KT	Rate	KT	Rate
40	1.916E−02	–	3.710E−04	–	6.514E−03	–	3.321E−05	–
80	1.042E−02	0.99	1.646E−04	1.25	3.239E−03	1.01	8.755E−06	1.92
160	5.576E−03	1.00	7.573E−05	1.15	1.607E−03	1.01	2.070E−06	2.08
320	2.955E−03	1.01	3.566E−05	1.10	7.718E−04	1.06	5.331E−07	1.96
640	1.536E−03	1.02	1.696E−05	1.08	3.961E−04	0.96	1.296E−07	2.04
1280	7.794E−04	1.05	8.034E−06	1.09	1.903E−04	1.06	3.407E−08	1.93

The mixture is composed by two fluids, the denser phase with density $\rho_q = 1000$ and the dispersed, less dense phase, with density $\rho_p = 1$, the gravitational acceleration is $g = -10$. Starting from the initial condition with $\alpha_p = \alpha_p^0$ and due to buoyancy effects the less dense phase moves upwards and the denser phase settles down at the bottom of the domain. The dynamics of the problem is governed by the relative velocity law, $v_{pq}(\alpha_p)$ given in Eq. (24).

Taking a one dimensional simplification it is easy to see that the center-of-volume velocity is everywhere zero, $\vec{v}_v = 0$ and the mass conservation equation for the dispersed phase, α_p, reduces to:

$$\frac{\partial \alpha_p}{\partial t} + \frac{\partial}{\partial z}[\alpha_p(1-\alpha_p)\,\vec{v}_{pq}] = 0. \tag{29}$$

Choosing $a = 1$ in the relative velocity law the resulting flux function and its derivative are given by:

$$\mathcal{F}(\alpha_p) = v_{rc}\,\alpha_p(1-\alpha_p)^2 \quad \mathcal{F}'(\alpha_p) = v_{rc}\,(1-\alpha_p)(1-3\,\alpha_p), \tag{30}$$

which is similar to the problem proposed by Nigam [48]. Starting from an initial condition given by $\alpha_p = 0.3$ with $v_{rc} = 1$ the analytical solution presents an upgoing shock indicated by (1) in Fig. 6(*a*) and a downgoing rarefaction-shock indicated by (2). Then, Fig. 6(*b*) presents the analytical solution for $t = 1$ and the corresponding numerical solution by the KTcFlux scheme in a domain of $h = 1$ with a mesh of 320 elements, using MinMod limiter showing good agreement. This example sets a trivial case for the KTcFlux scheme since the conservative flux at faces is identically zero, therefore the scheme reduces to the original KT scheme and does not require to solve the complete sets of equations given in Eq. (23). The results show that the proposed method recovers the characteristics of the original one.

As for the error analysis, it is presented in Table 2. This table shows the convergence rates for the complete solution in L^1 and *Lip*′ norms and the measures for the shock zone, taking $z < 0.6$. For the complete solution, both L^1 and *Lip*′ norms lead to first order convergence rates. The second order convergence rate is recovered when the error is measured only for the shock zone. From these results it is clear that using the *Lip*′ norm allows for recovering the convergence order only in discontinuities and not in rarefactions. Regarding the monotonicity and mass conservation errors, the maximum and minimum vales for α_q along time are, $\alpha_{q,\max} = 1$ and $\alpha_{q,\min} = 0$ and the difference at final time for integrated α_q with respect to the initial value is, $\Delta\alpha_q = -1.21 \times 10^{-11}$, showing an excellent performance.

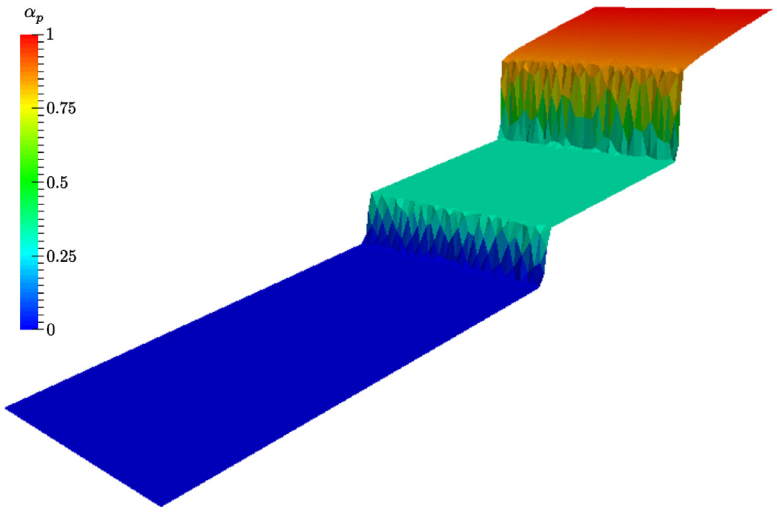

Fig. 7. Batch settling experiment, 2D KTcFlux solution.

A similar test can be set using a two dimensional domain with a height $h = 1$ and width $b = 0.3$ meshed with a non-structured triangulated mesh (size $\sim 1/200$). The boundary conditions at both lateral sides are set as periodic in order to recover a one dimensional solution. Fig. 7 presents the results using a Mimmod limiter showing again good agreement. It is important to remark that due to geometrical requirements of the OpenFOAM® libraries both meshes were really three dimensional, in the first case the elements were hexahedrons with two not-solved directions and in the second one the elements were wedges with one not-solved direction (perpendicular to the plane) [22]. The corresponding monotonicity and mass conservation errors, are, $\alpha_{q,\max} = 0.99$, $\alpha_{q,\min} = 0$ and $\Delta\alpha_q = 6.04 \times 10^{-13}$.

4.4. Bubble reactor

In this case a bubble plume of $\rho_p = 1$ is generated within a reactor with a denser fluid $\rho_q = 100$. The reactor is represented by a one dimensional model, the pure gas inlet $\alpha_{p,i} = 1$ is given at the bottom of the domain with $v_{p,i} = 0.25$. The reactor has a total height $h_T = 1$ and is filled with the denser fluid, $\alpha_q = 1$, until $h_0 = 0.5$ as is shown in Fig. 8(a). Since the problem has an inlet the center-of-volume velocity is not zero, but given by the value of the inlet boundary condition. Then, using the mass conservation equation for the mixture, $\partial u/\partial x = 0$, it follows that $u = v_{p,i} = 0.25$ for the whole domain. This case presents the next level of complexity regarding the values of u since it is constant but has a non-zero value and requires the action of the complete conservative solver to solve the system given by Eq. (23). The relative velocity law is selected as a constant, which is written for the continuous phase as:

$$v_{qp} = v_{rc}, \tag{31}$$

where the value of relative velocity constant, v_{rc}, is $v_{rc} = -1$. Therefore the mass conservation equation for the continuous phase is given by:

$$\frac{\partial \alpha_q}{\partial t} + \frac{\partial}{\partial z}(u\,\alpha_q) + \frac{\partial}{\partial z}[\alpha_q(1-\alpha_q)\,v_{rc}] = 0, \tag{32}$$

and the respective flux and flux derivative:

$$\mathcal{F}(\alpha_q) = u\,\alpha_q + v_{rc}\,\alpha_q(1-\alpha_q) \quad \mathcal{F}'(\alpha_q) = u + v_{rc}\,(1-2\,\alpha_q). \tag{33}$$

The graphs for the flux function and its derivative are presented in Fig. 8(b). In order to draw the convex hull it is required to know the states in α_q present within the reactor. Two of these states are given by the initial conditions of the reactor, $\alpha_q = 1$ (point B), for the zone filled with the denser fluid and $\alpha_q = 0$ (point C) for the region over the free surface. The third required state (point A) is given by the equilibrium between the inlet velocity of the gas phase and its velocity within the reactor, v_{pq}. It is clear that if v_{pq} is smaller than the inlet velocity a shock is created and a front of $\alpha_p = 1$ travels to the top displacing the fluid placed within the reactor. On the other hand, if $v_{pq} > v_{p,\,i}$ it implies that the gas travels faster within the reactor than in the inlet, therefore, the fraction of gas is reduced to an equilibrium value. In this case a rarefaction wave travels to the top of the reactor until reaching an steady state, where the reactor is filled by a mixture of gas and liquid and the new free surface position has changed. The equilibrium value for α_p, $\alpha_{p,\,a}$ is obtained by means of the conservation equation [23] and given by Eq. (34):

$$\alpha_{p,a} = \frac{v_{p,i}\,\alpha_{p,i}}{v_{rc}} \quad 0 \leqslant \alpha_{p,a} \leqslant 1, \tag{34}$$

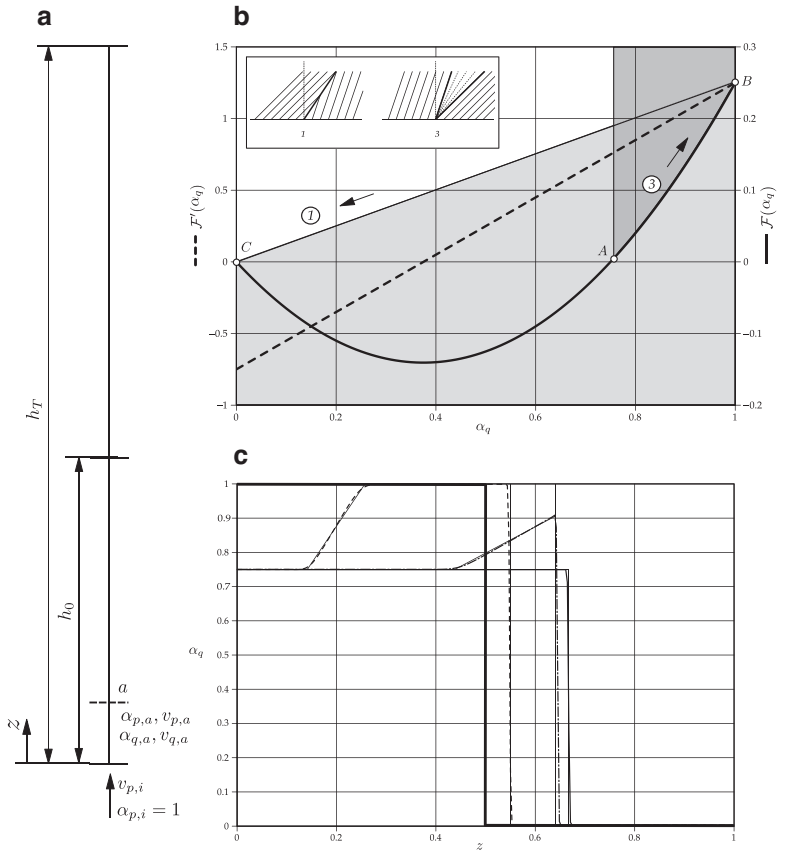

Fig. 8. One dimensional bubble reactor. *(a)* Domain and magnitudes; *(b)* $\mathcal{F}(\alpha_p)$, derivative, $\mathcal{F}'(\alpha_p)$ and convex hull plot; *(c)* ——— initial condition, KTcFlux solution with MinMod limiter for: — — — — $t = 0.2$, ——•—— $t = 0.6$, ——·—— $t = 2$. Thin continuous lines represent analytical solutions.

Table 3
Errors for bubble reactor problem.

N	Complete solution				Right going shock			
	L^1 error		*Lip*′ error		L^1 error		*Lip*′ error	
	KT	Rate	KT	Rate	KT	Rate	KT	Rate
40	1.318E−02	–	5.482E+00	–	1.334E−02	–	2.230E+00	–
80	6.642E−03	0.99	2.305E+00	1.25	6.651E−03	1.00	5.568E−01	2.00
160	3.324E−03	1.00	1.040E+00	1.15	3.312E−03	1.01	1.392E−01	2.00
320	1.650E−03	1.01	4.841E−01	1.10	1.643E−03	1.01	3.479E−02	2.00
640	8.117E−04	1.02	2.284E−01	1.08	8.086E−04	1.02	8.692E−03	2.00
1280	3.928E−04	1.05	1.076E−01	1.09	3.912E−04	1.05	2.167E−03	2.00

which for the present problem values gives $\alpha_{p,a} = 0.25$, $\alpha_{q,a} = 1 - 0.25 = 0.75$. Finally, since the fraction of liquid within reactor represents a fraction of $\alpha_{q,a} = 0.75$ in the steady-state it implies that the final height of the mixture reaches the value $h_f = h_0/\alpha_{q,a} = 0.5/0.75 = 0.66$. Having determined points *A*, *B* and *C* Fig. 8(b) shows that an upgoing rarefaction wave travels from bottom to top between points *A* and *B* [indicated by (3)] and then an upgoing shock between points *B* and *C*. The results are presented in Fig. 8(c) and were calculated using a MinMod limiter with a mesh of 320 elements. There, it is clear that the right going rarefaction fan and shock, as well as the equilibrium value $\alpha_{q,a} = 0.75$ and the final height of the mixture $h_f = 0.66$ are correctly captured.

The error analysis presented in Table 3 confirms that the method retains the convergence rates measured in the previous cases. Again, the presence of rarefactions (continuous solution with discontinuous derivative) leads the convergence to first order, even in *Lip*′ norm. Regarding the monotonicity and mass conservation errors, the maximum and minimum vales for α_q along time are, $\alpha_{q,\max} = 1$ and $\alpha_{q,\min} = -6.82 \times 10^{-28}$ and the difference at final time for integrated α_q with respect to the initial value is, $\Delta\alpha_q = -2.44 \times 10^{-11}$, showing an excellent performance.

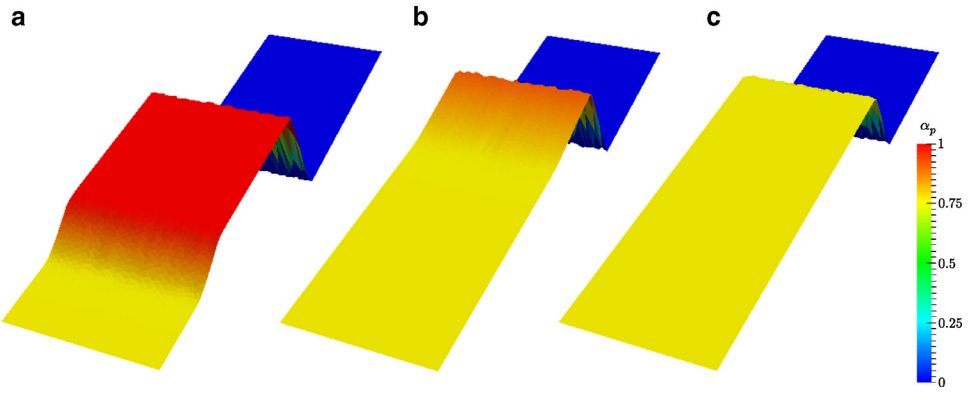

Fig. 9. Two dimensional bubble reactor. KTcFlux solution for: (a) $t = 0.2$, (b) $t = 0.6$ and (c) $t = 2$.

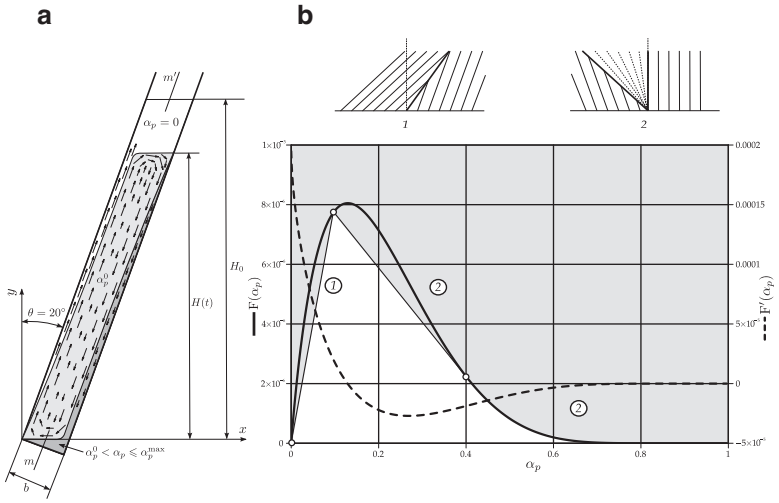

Fig. 10. (a) Geometry for Acrivos inclined sedimentation problem. (*b*) Flux initial condition, KTcFlux solution for: $t = 0.2$, $t = 0.6$, $t = 2$.

As in the settler case the reactor is solved in a two dimensional mesh in order to check the performance of the KTcFlux scheme in non-structured meshes. A triangulated mesh similar to one of the settler case is used running with MinMod limiter. As is presented in Fig. 9 the results are good and the scheme is able to capture the waves and the steady-state of the problem. The corresponding monotonicity and mass conservation errors, are, $\alpha_{q,\max} = 1$, $\alpha_{q,\min} = -1.31 \times 10^{-33}$ and $\Delta\alpha_q = 6.22 \times 10^{-15}$.

4.5. The Boycott effect

The effect of accelerated sedimentation of particles in a fluid using inclined plates is called the Boycott effect after Boycott [49] who was the first researcher who reported it. This phenomenon can be described by means of Fig. 10(a). If a mixture (α_p^0) is left to settle between parallel plates, Boycott observed that the sedimentation rate increases with the tilt angle, θ. The inclination of the plates shortens the sedimentation path of particles which aggregate on the upward-facing surface meanwhile a clean layer of liquid is formed below the downward-facing surface ($\alpha_p = 0$). The sediments creep to the bottom and the clear liquid goes upwards. This process gives place to a clear liquid layer at the top and sediment packed layer at the bottom of the domain ($\alpha_p^0 < \alpha_p \leqslant \alpha_p^{\max}$). Within the mixture core a big vortex is formed which sets a completely non-uniform velocity field in the settler.

Some years later Ponder [50], and Nakamura and Kuroda [51] presented the first quantitative prediction using a kinematic description (PNK model). This model was subsequently improved by Acrivos and Herbolzheimer [52] using asymptotic analysis, obtaining very accurate predictions to their experiments. The objective of this example is to test the KTcFlux scheme in the simulation of the Boycott effect comparing the results of a numerical solution for the Acrivos model and the respective experiments. This case allows to test the KTcFlux scheme in a case with temporally and spatially variable centered face fluxes.

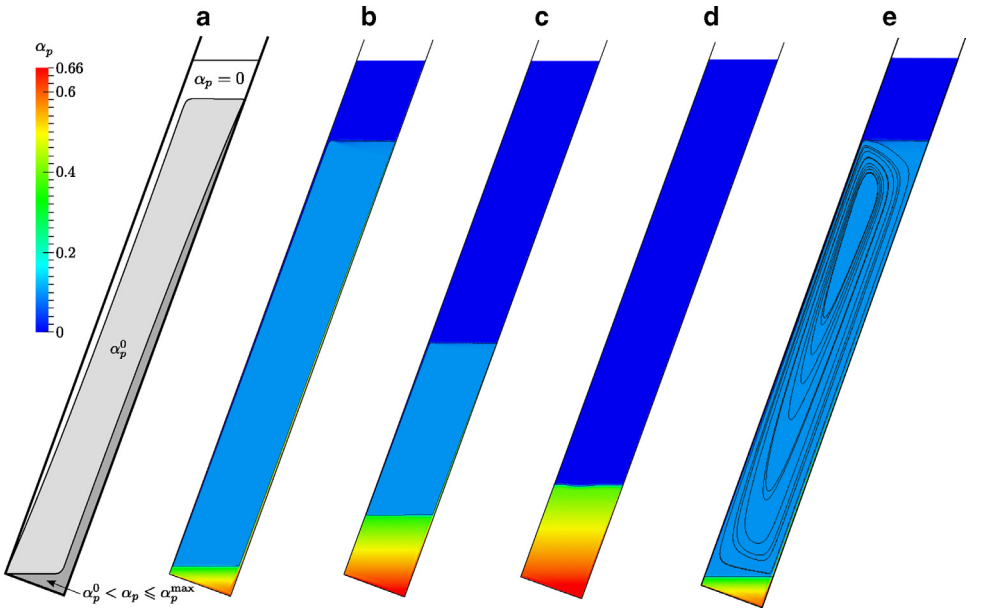

Fig. 11. Solutions for the Acrivos and Herbolzheimer problem. (a) Model solution showing the three characteristic zones $\alpha_p = 0$: clear water, α_p^0: initial mixture and $\alpha_p^0 < \alpha_p \leqslant \alpha_p{}^{max}$: packed zone. Solutions at (b) $t = 220$, (c) $t = 900$, (d) $t = 1800$. (e) Streamlines for $t = 220$.

Therefore, the test is set using a separation between plates, $b = 0.05$, the initial height of the mixture is, $H_0 = 0.4$. The densities are $\rho_q = 992$ for the fluid and $\rho_p = 2420$ for the particles. The mixture viscosity is calculated by Mooney's law [53]:

$$\frac{\mu_m}{\mu_q} = e^{(K_1\alpha_p)/(1-K_2\alpha_p)}, \tag{35}$$

where $\mu_q = 0.0677$, $K_1 = 1.66$ and $K_2 = 1$. The sedimentation velocity is calculated as:

$$\vec{v}_{pq} = \vec{v}_0\, f(\alpha_p) = \frac{2}{9} d^2 (\rho_p - \rho_q)\, \vec{g}/\mu_q f(\alpha_p), \tag{36}$$

where $\vec{v}_0$ is the settling velocity of the individual particles given by the Stokes' law (diameter, $d = 137 \times 10^{-6}$), $\vec{g} = (0, -10, 0)$ is the gravitational acceleration and $f(\alpha_p)$ is a monotonically decreasing hindrance function which takes into account the effect of sediment packing in the sedimentation velocity [54]:

$$f(\alpha_p) = \frac{(1-\alpha_p)^2}{(1+\alpha_p^{1/3})\, e^{\frac{5\alpha_p}{3(1-\alpha_p)}}}. \tag{37}$$

In addition, Fig. 10(*b*) presents the flux function and flux derivative for the case. The flux function presents almost zero slope at $\alpha_p \sim 0.7$ which implies that no further sedimentation is present beyond this packing value. Since the example starts with $\alpha_p = 0.1$, a traveling shock wave is present in the clear liquid interface at the top, meanwhile at the bottom a shock-rarefaction wave is developed until reaching the maximum packing. This last wave evolves from $\alpha_p = 0.1$ to $\alpha_p = 0.4$ as a shock and then to $\alpha_p \sim 0.7$ as a rarefaction. The flux function is calculated using the assumption of $\vec{v}_m = 0$ in the top clear water layer, at the sedimented layer and near the horizontal interphases [23,52] and plotted against α_p values along $m - m'$ line (see Fig. 10(*a*).

The case is set with structured meshes of hexahedral elements including a grading towards the downward-facing surface in order to better represent the clear water slit below it. Three meshes are used: Mesh 1, 60 by 200 elements; Mesh 2: 120 by 400 elements and Mesh 3: 240 by 800 elements. The KTcFlux scheme with MinMod reconstruction is used to solve the equation for α_p. Qualitative results are presented in Fig. 11. The Fig. 11(a) shows the model solution with the three zones explained in the introduction of the problem, the initial mixture layer (α_p^0), the clear water layer ($\alpha_p = 0$), and the packed zone ($\alpha_p^0 < \alpha_p \leqslant \alpha_p{}^{max}$). Then, solutions for $t = 220$, $t = 900$ and $t = 1800$ are presented in figures Fig. 11(b) and (d), these figures show that the structures described by Acrivos and Herbolzheimer are present: a thin clear slit below the downward-facing surface, a traveling front with sharp interface going from top to bottom, a packed bed in the upward-facing surface and the accumulation of the sediments in the bottom of the domain with variable concentration. Finally, Fig. 11(e) presents the streamlines generated by the velocity field within the initial mixture zone, clearly the vortex expected for this zone is present.

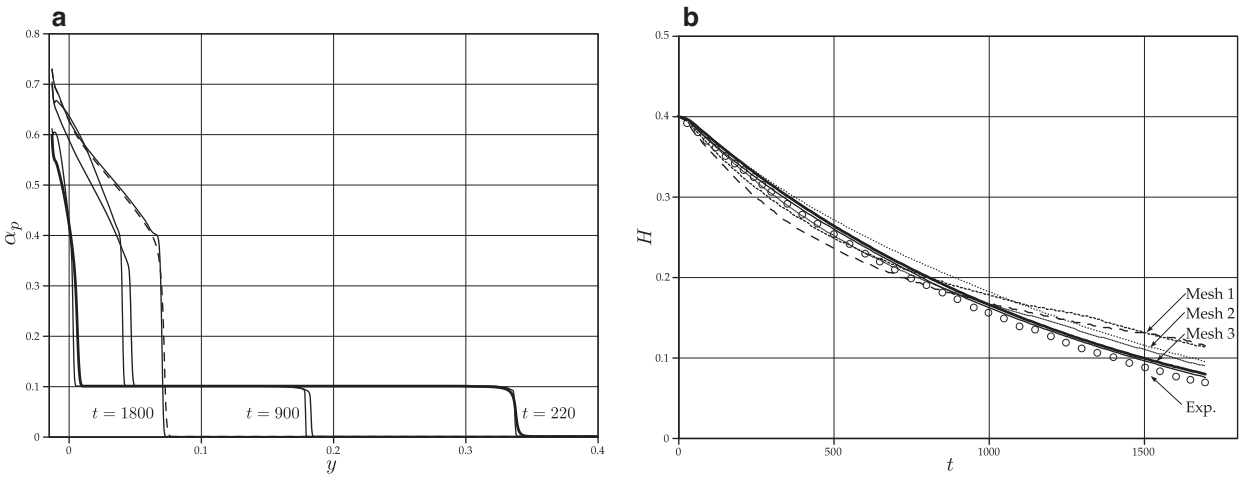

Fig. 12. Solution for the Acrivos and Herbolzheimer problem. (a) Profiles of sediments concentration, α_p, at different times; (b) temporal evolution of the clear water front for different meshes. Thick lines, MinMod limiter, thin lines van Leer limiter.

Next, Fig. 12 shows quantitative results for the sediments concentration and the dynamics of the clear water front for the finest mesh (Mesh 3). Fig. 12(a) shows the evolution of the concentration, α_p, for times $t = 220$, $t = 900$ and $t = 1800$, along line $m - m'$ [see Fig. 10(a)]. The results confirm the presence of a shock traveling from top to bottom and a variable concentration of sediments at the bottom of the domain. The sediments layer growths, as is expected, by a rarefaction and then a shock traveling upwards, the shock evolves from $\alpha_p \sim 0.4$ to $\alpha_p^0 = 0.1$ as is indicated in the convex hull of Fig. 10(b). Then, Fig. 12(b) presents a comparison of the evolution of the clear water front over time for the three meshes used here and the experimental results of Acrivos and Herbolzheimer. This figure confirms mesh convergent results showing excellent agreement with the experimental data for the finest mesh. As additional results the same calculations were done with the van Leer limiter in order to improve the shock wave spatial resolution and time evolution.

Finally Fig. 13 presents a comparison of results for $t = 30$ with both interpolated velocities method and the face fluxes method. Fig. 10(a) and (b) compare the dispersed phase concentration for both methods. It is clear that the use of the interpolated velocities method leads to oscillations in the concentration. Here it is also important to remark that the complete range of values for α_p is $[-0.5, 0.47]$, the actual range in the figure is selected in order to see the oscillations. Values below zero are unphysical and cause the simulation to stop at $t \sim 32.9$. The results for velocity fields presented in Fig. 10(c) and (d) confirm the conclusions obtained from the first figures, a disturbed field is obtained by the interpolated velocities method which differs from the ordered pattern obtained by the face fluxes method.

Regarding the monotonicity and mass conservation errors, the maximum and minimum vales for α_q along time are, $\alpha_{q,\max} = 0.73$ and $\alpha_{q,\min} = -1.2 \times 10^{-4}$ and the difference at final time for integrated α_q with respect to the initial value is, $\Delta\alpha_q = 2.38 \times 10^{-18}$, showing an excellent performance.

5. Conclusions

An extension of the Kurganov and Tadmor (KT) central scheme was presented which allows for its use with conservative incompressible cell-centered Finite Volume solvers (KTcFlux) in polyhedral meshes obtaining monotone solutions. The inclusion of conservative fluxes was derived from the work of Abreu et al. whereas the application to polyhedral meshes followed the method of face-by-face reconstruction of Greeenshields et al.

Using the fluxes obtained from the pressure–velocity coupling is a key concept to preserve the monotonicity of the solution. Improvements with respect to calculating the fluxes using the original KT scheme were illustrated in a linear advection problem.

The proposed scheme was then applied to a mixture multiphase solver using OpenFOAM® technology and used in a series of sedimentation cases. The first example was a batch sedimentation case with null face flux, the numerical solutions obtained showed excellent agreement with their analytical counterparts both in one and two dimensions and using unstructured meshes. The errors for the one dimensional case were measured confirming second order convergence. The next step was to solve a bubble reactor which allowed to test the pressure–velocity coupling and the KTcFlux scheme working together. Again, the numerical results showed to be in agreement with analytical solution, retaining the order of convergence.

Finally, a case of batch sedimentation between inclined plates was solved. This problem exhibits full two-dimensional behavior and requires the solver to capture several structures of the flow: the clear water slit below the downward-facing surface, the downgoing discontinuity (shock) between the clear water and mixture core, the sediment packed layer on the upward-facing surface, the accumulation of sediments at the bottom of the domain with variable concentration and the vortex within the mixture core. All these structures were captured, which allowed for a qualitative evaluation of the

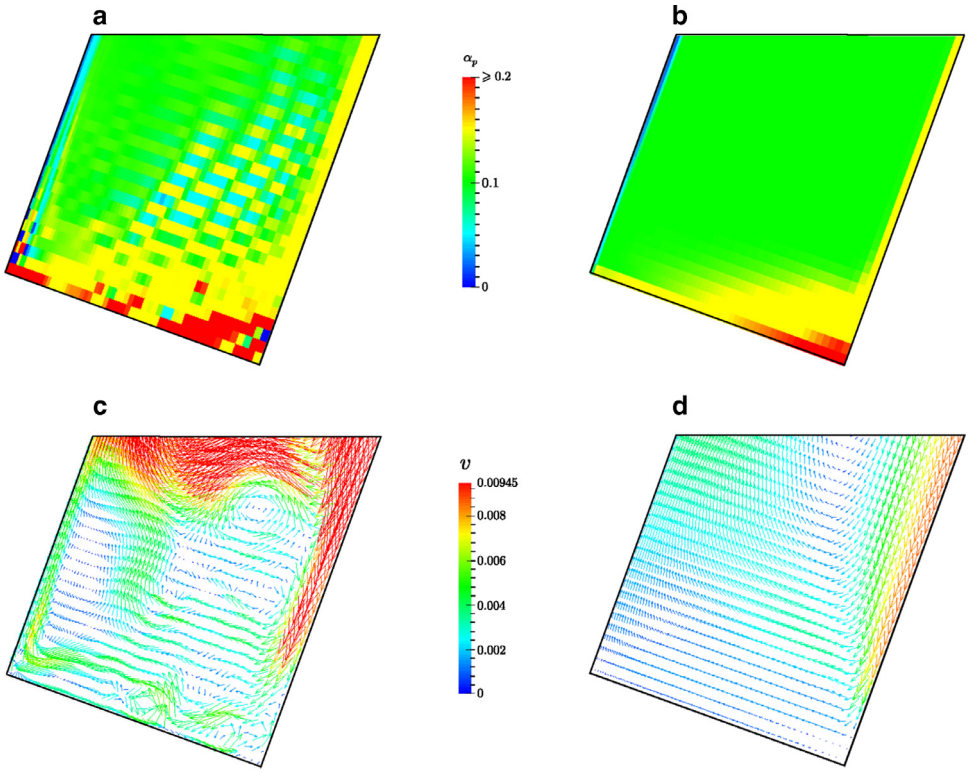

Fig. 13. Comparison of solution for the Acrivos and Herbolzheimer problem using the interpolated velocities method and the face fluxes method. (a) Concentration for α_p with the interpolated velocities method; (b) similar results using the face fluxes method (scale range restricted to $[0, 0.2]$, complete range is $[-0.5, 0.47]$); (c) velocity field using the interpolated velocities method; (d) similar results using the face fluxes method.

performance of the proposed scheme. As a quantitative validation the evolution of the downgoing shock of clear water along time was compared with experimental results showing excellent agreement. This case was also useful to perform additional comparisons of the face velocities calculation. The use of conservative fluxes from the pressure–velocity coupling loop gave monotone results and allowed to obtain an accurate flow field.

All the examples confirmed that the KTcFlux scheme can be used in the context of incompressible solvers in polyhedral meshes, presenting excellent capturing of waves and guaranteeing local and global monotonicity.

Acknowledgments

The authors wish to give thanks to CONICET, Universidad Nacional del Litoral (grant CAI+D 65333, 2009) and ANPCyT (grant PICT 1645, BID 2008) for their financial support. The collaboration between CIMEC and ICMC has been possible thanks to the CONICET/FAPESP International Cooperation Agreement. Gustavo C. Buscaglia acknowledges support from FAPESP and CNPq. Part of the computing was done in Coyote cluster which was funded by CONICET (grants PIP 0341, 2009 and PIP 2956, 2009) and ANPCyT (grant PICT 2492, 2010).

The computation of the Lip' norm errors (Lipschitz dual seminorm) was possible by the assistance of professors Alexander Kurganov (Department of Mathematics, Tulane University, USA) and Pedro Morín (IMAL, CONICET, Argentina).

An special acknowledgment is given to OpenFOAM®, gdb, octave, Inkscape and Paraview® developers and users community for their contribution to free software.

Appendix A. Kurganov and Tadmor central scheme derivation

As a reference for the reader the derivation of the one dimensional semi-discrete form of the original Kurganov and Tadmor scheme [4] is recalled, adding some useful insights. In order to set a basis for the time integration procedures used it is worthy to recall some definitions (see Fig. 14):

- u: is the continuous function being integrated in time and space (scalar case of $\vec{u}$);
- $\overline{u}$: is a piecewise constant approximation of u obtained by the sliding average presented in Eq. (A.1)
- $\tilde{u}$: is a piecewise linear approximation of u defined in Eq. (A.2).

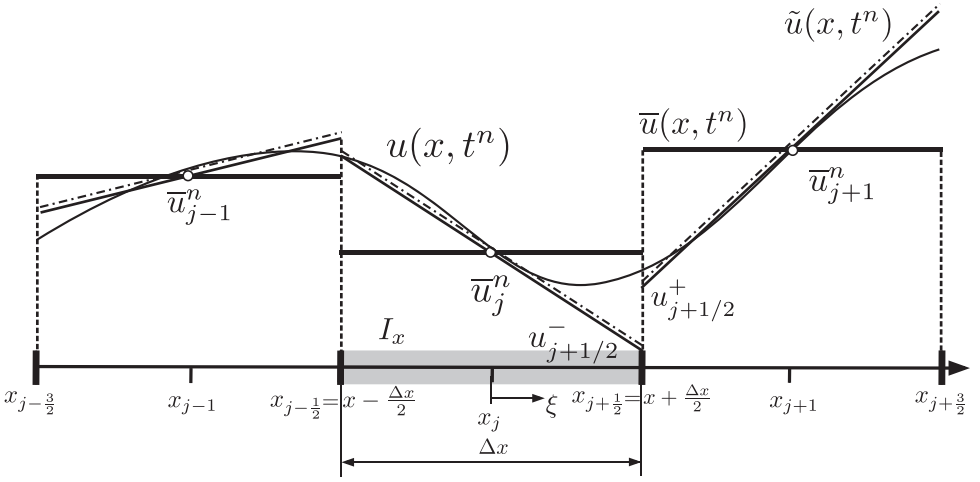

Fig. 14. Original continuous function u (continuous thin line), $\overline{u}$ piecewise constant approximation (continuous thick line), $\tilde{u}$ piecewise linear approximation (dash dotted line). The discretization cell is hatched in gray.

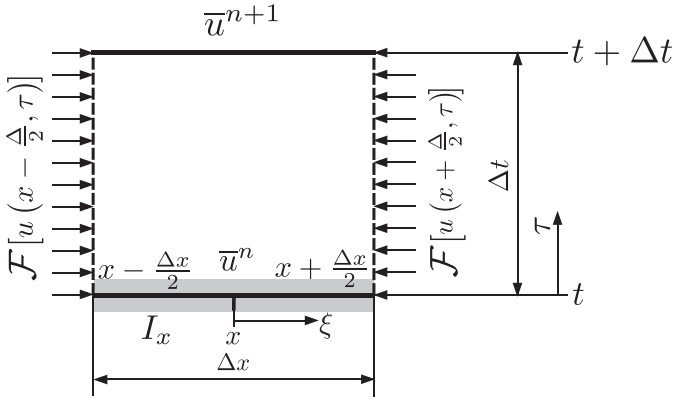

Fig. 15. Integration domain along x and t for $\overline{u}$.

$$\overline{u}(x,t^n)=\frac{1}{|I_x|}\int_{I_x}u(\xi,t)\,d\xi,\qquad I_x=\left\{\xi:|\xi-x|\leqslant\frac{\Delta x}{2}\right\} \tag{A.1}$$

$$\tilde{u}(x,t^n)=\sum_j\left[\overline{u}^n_j+(u_x)^n_j(x-x_j)\right]\mathbf{1}_{[x_{j-1/2},x_{j+1/2}]},\quad x_{j\pm1/2}=x_j+\frac{\Delta x}{2} \tag{A.2}$$

where $\mathbf{1}_{[x_{j-1/2},x_{j+1/2}]}$ is the indicator function which has a value of 1 within the interval given in the sub-index and zero otherwise. The calculation of the piecewise linear approximation requires the values of $(u_x)^n_j$ which are approximations to the exact derivatives $u_x(x_j,\,t^n)$ computed from the cell averages $\overline{u}$. The computation of such approximate derivatives relies on TVD methods [26]. In addition, to evolve $\overline{u}$ in time the integration presented in Eq. (A.3) is done over the rectangle $I_x\times[t,t+\Delta t]$ (see Fig. 15).

$$\overline{u}(x,t+\Delta t)=\overline{u}(x,t^n)-\frac{1}{\Delta x}\left[\int_{\tau=t}^{t+\Delta t}\mathcal{F}\left(u\left(x+\frac{\Delta x}{2},\tau\right)\right)d\tau-\int_{\tau=t}^{t+\Delta t}\mathcal{F}\left(u\left(x-\frac{\Delta x}{2},\tau\right)\right)d\tau\right] \tag{A.3}$$

Finally, this scheme relies on a stabilization for the advective terms based on the *local* speeds of wave propagation, which for the most practical applications can be defined as in Eq. (A.4).

$$a^n_{j+1/2}:=\max\left\{\rho\left(\frac{\partial\mathcal{F}}{\partial u}\left(u^-_{j+1/2}\right)\right),\rho\left(\frac{\partial\mathcal{F}}{\partial u}\left(u^+_{j+1/2}\right)\right)\right\} \tag{A.4}$$

where ρ is the spectral radius of the $\frac{\partial\mathcal{F}}{\partial u}$ matrix at each side of a face and $u^-_{j+1/2}$, $u^+_{j+1/2}$ are the values of u at both sides of the $x_{j+\frac{1}{2}}$ cell interface.

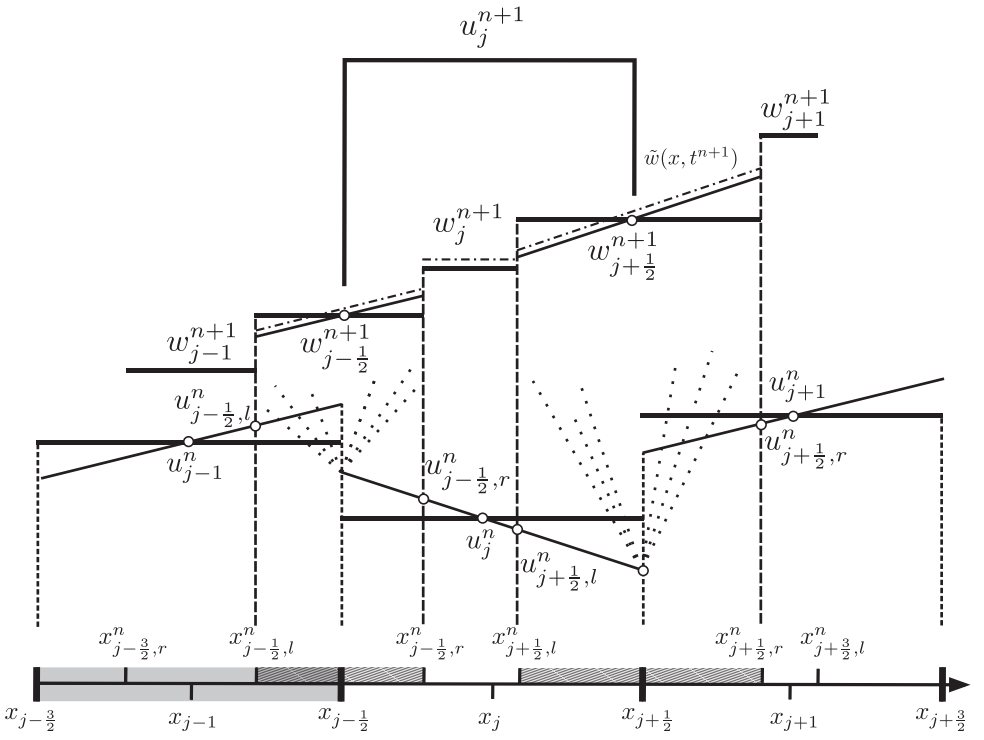

Fig. 16. Geometrical basis for central differencing scheme [Adapted from [4]].

The procedure starts integrating over intervals placed around the cell interfaces; these integration intervals are delimited by long-dashed lines and hatched with lines in Fig. 16, meanwhile the cells of the base mesh are hatched in gray. This integration gives the values of the w^{n+1} function from the original solution values u^n. Here it is important to note that the w^{n+1} values are placed at the interfaces and not in the original cell centers leading to a staggered mesh; this idea is exploited by the Nessyahu and Tadmor [2] scheme. This staggered solution is not convenient therefore a new integration is done through a $\tilde{w}^{n+1}$ function, defined over the jth cell and its neighbors with a width defined by the local speeds, as is shown with dash-dotted line in Fig. 16. As a result of this last integration the time updated values of u^n are found as u^{n+1}. As is explained in the work of Kurganov and Tadmor, the values of the continuous function being integrated, u, differ in a negligible second order term with cell averages, $\bar{u}$, then the overbar is drop hereinafter.

Then, Step 1 for the construction of the scheme is to integrate over the interval $[x^n_{j+1/2,l}, x^n_{j+1/2,r}] \times [t^n, t^{n+1}]$ (see the detailed Fig. 17), where the extrema of the spatial interval are defined as: $x^n_{j+1/2,l} := x_{j+1/2} - a^n_{j+1/2}\Delta t$ and $x^n_{j+1/2,r} := x_{j+1/2} + a^n_{j+1/2}\Delta t$. Then, if $\Delta x_{j+1/2} := x^n_{j+1/2,r} - x^n_{j+1/2,l}$ denotes the width of the Riemann fan originated at $x_{j+1/2}$; the average of u within this interval is given by Eq. (A.5):

$$\begin{aligned} w^{n+1}_{j+1/2} &= \frac{1}{\Delta x_{j+1/2}} \int_{x^n_{j+1/2,l}}^{x^n_{j+1/2,r}} u(\xi, t^{n+1}) d\xi \\ &= \frac{1}{\Delta x_{j+1/2}} \int_{x^n_{j+1/2,l}}^{x^n_{j+1/2,r}} \tilde{u}(\xi, t^n) d\xi - \frac{1}{\Delta x_{j+1/2}} \int_{t^n}^{t^{n+1}} \left\{ \mathcal{F}\left[u(x^n_{j+1/2,r}, \tau)\right] - \mathcal{F}\left[u(x^n_{j+1/2,l}, \tau)\right] \right\} d\tau \\ &= \frac{u^n_j + u^n_{j+1}}{2} + \frac{\Delta x - a^n_{j+1/2}\Delta t}{4} \left[(u_x)^n_j - (u_x)^n_{j+1} \right] \\ &\quad - \frac{1}{2a^n_{j+1/2}\Delta t} \int_{t^n}^{t^{n+1}} \left\{ \mathcal{F}\left[u\left(x^n_{j+1/2,r}, \tau\right)\right] - \mathcal{F}\left[u\left(x^n_{j+1/2,l}, \tau\right)\right] \right\} d\tau \end{aligned} \tag{A.5}$$

The same is done for the interval $[x^n_{j-1/2,l}, x^n_{j-1/2,r}] \times [t^n, t^{n+1}]$ giving which is shown in Eq. (A.6)

$$\begin{aligned} w^{n+1}_{j-1/2} &= \frac{u^n_j + u^n_{j-1}}{2} + \frac{\Delta x - a^n_{j-1/2}\Delta t}{4} \left[(u_x)^n_{j-1} - (u_x)^n_j \right] \\ &\quad - \frac{1}{2a^n_{j-1/2}\Delta t} \int_{t^n}^{t^{n+1}} \left\{ \mathcal{F}\left[u\left(x^n_{j-1/2,r}, \tau\right)\right] - \mathcal{F}\left[u\left(x^n_{j-1/2,l}, \tau\right)\right] \right\} d\tau \end{aligned} \tag{A.6}$$

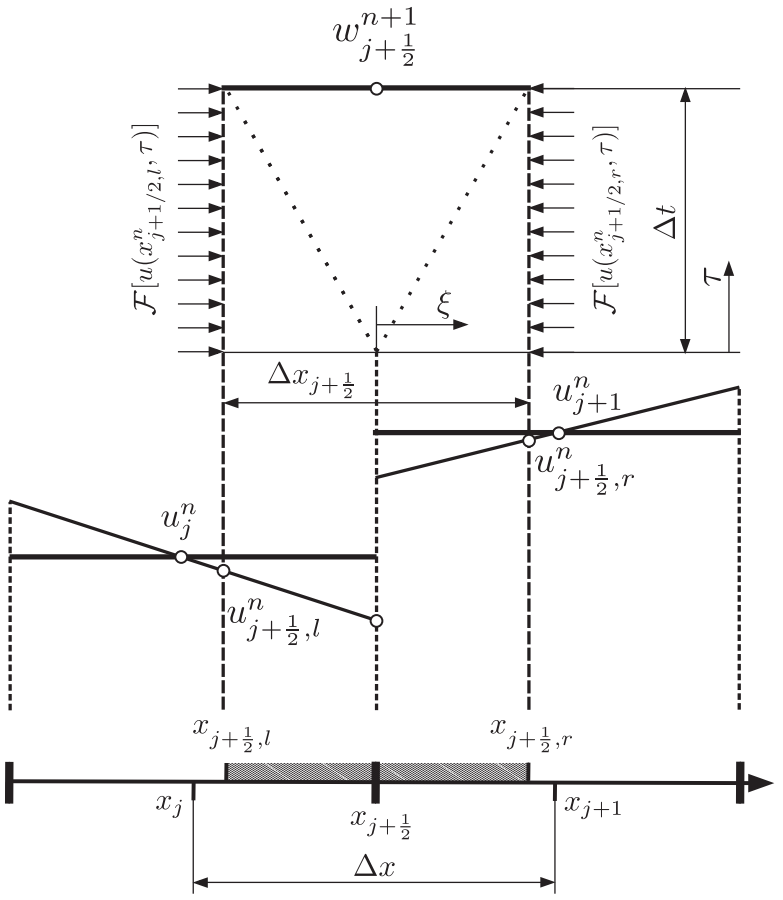

Fig. 17. Detail of Fig. 16 to show the integration over the cell interfaces.

Similarly taking $\Delta x_j := x^n_{j+1/2,l} - x^n_{j-1/2,r} = \Delta x - \Delta t(a^n_{j-1/2} + a^n_{j+1/2})$ which is the width of the strip around x_j where there is no influence of the Riemann fans from neighboring points, the average is given by Eq. (A.7)

$$\begin{aligned} w^{n+1}_j &= \frac{1}{\Delta x_j}\int_{x^n_{j-1/2,r}}^{x^n_{j+1/2,l}} \tilde{u}(\xi, t^{n+1})d\xi \\ &= u^n_j + \frac{\Delta t}{4}\left(a^n_{j-1/2} - a^n_{j+1/2}\right)(u_x)^n_j - \frac{1}{\Delta x_j}\int_{t^n}^{t^{n+1}} \left\{\mathcal{F}\left[u\left(x^n_{j+1/2,l},\tau\right)\right] - \mathcal{F}\left[u\left(x^n_{j-1/2,r},\tau\right)\right]\right\}d\tau \end{aligned} \tag{A.7}$$

Finally, using the midpoint rule it is possible to approximate the integrals over the flux in Eqs. (A.5)–(A.7) giving the desired cell averages at $t = t^{n+1}$ in Eq. (A.8)

$$\begin{aligned} w^{n+1}_{j+1/2} &= \frac{u^n_j + u^n_{j+1}}{2} + \frac{\Delta x - a^n_{j+1/2}\Delta t}{4}\left[(u_x)^n_j - (u_x)^n_{j+1}\right] - \frac{1}{2a^n_{j+1/2}}[\mathcal{F}(u^{n+1/2}_{j+1/2,r}) - \mathcal{F}(u^{n+1/2}_{j+1/2,l})] \\ w^{n+1}_{j-1/2} &= \frac{u^n_j + u^n_{j-1}}{2} + \frac{\Delta x - a^n_{j-1/2}\Delta t}{4}\left[(u_x)^n_{j-1} - (u_x)^n_j\right] - \frac{1}{2a^n_{j-1/2}}[\mathcal{F}(u^{n+1/2}_{j-1/2,r}) - \mathcal{F}(u^{n+1/2}_{j-1/2,l})] \\ w^{n+1}_j &= u^n_j + \frac{\Delta t}{2}\left(a^n_{j-1/2} - a^n_{j+1/2}\right)(u_x)^n_j - \frac{\lambda}{1-\lambda(a^n_{j-1/2} + a^n_{j+1/2})}[\mathcal{F}(u^{n+1/2}_{j+1/2,l}) - \mathcal{F}(u^{n+1/2}_{j-1/2,r})] \end{aligned} \tag{A.8}$$

where $\lambda = \Delta t/\Delta x$. Now, it is necessary to evaluate $u^{n+1/2}_{j\pm1/2,l}$ and $u^{n+1/2}_{j\pm1/2,r}$. This goal is achieved using the original hyperbolic equation and Taylor expansions giving the results presented in Eq. (A.9)

$$\begin{aligned} u^{n+1/2}_{j\pm1/2,l} &:= u^n_{j\pm1/2,l} - \frac{\Delta t}{2}\mathcal{F}(u^n_{j\pm1/2,l})_x \\ u^{n+1/2}_{j\pm1/2,r} &:= u^n_{j\pm1/2,r} - \frac{\Delta t}{2}\mathcal{F}(u^n_{j\pm1/2,r})_x \end{aligned} \tag{A.9}$$

where,

$$u^n_{j+1/2,l} = u^n_j + \Delta x(u_x)^n_j\big(1/2 - \lambda\, a^n_{j+1/2}\big); \quad u^n_{j+1/2,r} = u^n_{j+1} - \Delta x(u_x)^n_{j+1}$$
$$u^n_{j-1/2,l} = u^n_{j-1} + \Delta x(u_x)^n_{j-1}\big(1/2 - \lambda\, a^n_{j-1/2}\big); \quad u^n_{j-1/2,r} = u^n_j - \Delta x(u_x)^n_j\big(1/2 - \lambda\, a^n_{j-1/2}\big) \tag{A.10}$$

At this point, the function u has evolved in time to the approximate cell averages $w^{n+1}_{j-1/2}$, w^{n+1}_j and $w^{n+1}_{j+1/2}$ which are located in a new staggered mesh. In order to obtain a solution over the original mesh the solution is newly averaged using a piecewise-linear reconstruction $\tilde{w}(x, t^{n+1})$ based on the w's (see Fig. 16, dash-dotted line). This reconstruction is defined by Eq. (A.11)

$$\begin{aligned}\tilde{w}(x, t^{n+1}) : = &\Big[w^{n+1}_{j-1/2} + (u_x)^{n+1}_{j-1/2}(x - x_{j-1/2})\Big]\mathbf{1}_{[x^n_{j-1/2,l}, x^n_{j-1/2,r}]} + w^{n+1}_j \mathbf{1}_{[x^n_{j-1/2,r}, x^n_{j+1/2,l}]} \\ &+ \Big[w^{n+1}_{j+1/2} + (u_x)^{n+1}_{j+1/2}(x - x_{j+1/2})\Big]\mathbf{1}_{[x^n_{j+1/2,l}, x^n_{j+1/2,r}]}\end{aligned} \tag{A.11}$$

and the required $(u_x)^{n+1}_{j-1/2}$, $(u_x)^{n+1}_{j+1/2}$ slopes are given by a TVD limiter from the values of the approximate cell averages w^{n+1}, in the case of the original KT scheme it uses MinMod [45] as the limiter. Therefore, doing the average as in Eq. (A.12)

$$\begin{aligned}u^{n+1}_j = \frac{1}{\Delta x}\int_{x_{j-1/2}}^{x_{j+1/2}} \tilde{w}(\xi, t^{n+1})\, d\xi = \frac{1}{\Delta x}\Big\{&\Delta x_j\Big[w^{n+1}_j\Big] + \Delta x_{j+1/2}\Big[w^{n+1}_{j+1/2} + (u_x)^{n+1}_{j+1/2}(x - x_{j+1/2})\Big] \\ &+ \Delta x_{j-1/2}\Big[w^{n+1}_{j-1/2} + (u_x)^{n+1}_{j-1/2}(x - x_{j-1/2})\Big]\Big\}\end{aligned} \tag{A.12}$$

and re-arranging finally gives that it is shown in Eq. (A.13)

$$\begin{aligned}u^{n+1}_j = &\lambda\, a^n_{j-1/2} w^{n+1}_{j-1/2} + \Big[1 - \lambda(a^n_{j-1/2} + a^n_{j+1/2})\Big]w^{n+1}_j + \lambda\, a^n_{j+1/2} w^{n+1}_{j+1/2} \\ &+ \frac{\Delta x}{2}\Big[(\lambda a^n_{j-1/2})^2 (u_x)^{n+1}_{j-1/2} - (\lambda a^n_{j+1/2})^2 (u_x)^{n+1}_{j+1/2}\Big]\end{aligned} \tag{A.13}$$

This final expression is known as the *Kurganov and Tadmor fully discrete second order* scheme. The piecewise reconstruction used ensures the obtained second-order accuracy [27]. In order to obtain a semi-discrete of this scheme u^n_j is subtracted to Eq. (A.13) and then divided by Δt to give which is shown in Eq. (A.14). There, the terms which result to be $\mathcal{O}(\lambda)$ are not explicitly written.

$$\begin{aligned}\frac{u^{n+1}_j - u^n_j}{\Delta t} &= \frac{a^n_{j-1/2}}{\Delta x} w^{n+1}_{j-1/2} + \left(\frac{1}{\Delta t} - \frac{a^n_{j-1/2} + a^n_{j+1/2}}{\Delta x}\right) w^{n+1}_j + \frac{a^n_{j+1/2}}{\Delta x} w^{n+1}_{j+1/2} - \frac{1}{\Delta t} u^n_j + \mathcal{O}(\lambda) \\
&= \frac{a^n_{j-1/2}}{2\Delta x}(u^n_{j-1} + u^n_j) + \frac{1}{4} a^n_{j-1/2}((u_x)^n_{j-1} - (u_x)^n_j) - \frac{1}{2\Delta x}[\mathcal{F}(u^{n+1/2}_{j-1/2,r}) - \mathcal{F}(u^{n+1/2}_{j-1/2,l})] \\
&\quad - \frac{a^n_{j-1/2} + a^n_{j+1/2}}{\Delta x} u^n_j + \frac{1}{2}(a^n_{j-1/2} - a^n_{j+1/2})(u_x)^n_j \\
&\quad - \frac{1}{\Delta x}[\mathcal{F}(u^{n+1/2}_{j+1/2,l}) - \mathcal{F}(u^{n+1/2}_{j-1/2,r})] - \frac{1}{\Delta x}[v^{n+1/2}_{j+1/2,l} u^{n+1/2}_{j+1/2,l} - v^{n+1/2}_{j-1/2,r} u^{n+1/2}_{j-1/2,r}] \\
&\quad + \frac{a^n_{j+1/2}}{2\Delta x}(u^n_j + u^n_{j+1}) + \frac{1}{4} a^n_{j+1/2}((u_x)^n_j - (u_x)^n_{j+1}) - \frac{1}{2\Delta x}[\mathcal{F}(u^{n+1/2}_{j+1/2,r}) - \mathcal{F}(u^{n+1/2}_{j+1/2,l})] + \mathcal{O}(\lambda) \\
&= \frac{1}{2\,\Delta x}\Bigg\{-\Big[\big(\mathcal{F}(u^{n+1/2}_{j+1/2,r}) + \mathcal{F}(u^{n+1/2}_{j+1/2,l})\big) - \big(\mathcal{F}(u^{n+1/2}_{j-1/2,r}) + \mathcal{F}(u^{n+1/2}_{j-1/2,l})\big)\Big] \\
&\quad + \frac{a^n_{j+1/2}}{\Delta x}\left[\left(u^n_{j+1} - \frac{\Delta x}{2}(u_x)^n_{j+1}\right) - \left(u^n_j + \frac{\Delta x}{2}(u_x)^n_j\right)\right] \\
&\quad - \frac{a^n_{j-1/2}}{\Delta x}\left[\left(u^n_j - \frac{\Delta x}{2}(u_x)^n_j\right) - \left(u^n_{j-1} + \frac{\Delta x}{2}(u_x)^n_{j-1}\right)\right]\Bigg\} + \mathcal{O}(\lambda)\end{aligned} \tag{A.14}$$

In order to obtain the semi-discrete form the limit when $\Delta t \to 0$ is taken. The first consequence is that the width of the staggered cells $\Delta x_{j+\frac{1}{2}}$ approaches zero (see Fig. 17), and the position of the sides of these cells, $x_{j+\frac{1}{2},r}$ and $x_{j+\frac{1}{2},l}$ approximate $x_{j+\frac{1}{2}}$, i.e. the intercell position of the original mesh. In addition, using Eq. (A.9) the midvalues result to be which is shown in Eq. (A.15)

$$\begin{aligned}u^{n+1/2}_{j+1/2,r} &\to u_{j+1}(t) - \frac{\Delta x}{2}(u_x)_{j+1}(t) =: u^+_{j+1/2}(t) \\
u^{n+1/2}_{j+1/2,l} &\to u_j(t) - \frac{\Delta x}{2}(u_x)_j(t) =: u^-_{j+1/2}(t)\end{aligned} \tag{A.15}$$

where $u^+_{j+1/2}$ and $u^-_{j+1/2}$ are reconstructed using the numerical slopes $(u_x)(t)$. The final form of the semi-discrete scheme is shown in Eq. (A.16)

$$\frac{d}{dt}u_j(t) = -\frac{\left(\mathcal{F}(u^+_{j+1/2}) + \mathcal{F}(u^-_{j+1/2,})\right) - \left(\mathcal{F}(u^+_{j-1/2}) + \mathcal{F}(u^-_{j-1/2})\right)}{2\Delta x} + \frac{1}{2\Delta x}\left\{a_{j+1/2}(t)[u^+_{j+1/2}(t) - u^-_{j+1/2}(t)] - a_{j-1/2}(t)[u^+_{j-1/2}(t) - u^-_{j-1/2}(t)]\right\} \tag{A.16}$$

The obtained scheme admits the conservative form as the original KT method, which is shown in Eq. (A.17)

$$\frac{d}{dt}u_j(t) = -\frac{C_{j+1/2}(t) - C_{j-1/2}(t)}{\Delta x} \tag{A.17}$$

where $C_{j+1/2}(t)$ is a numerical flux defined as in Eq. (A.18)

$$C_{j+1/2(t)} = \frac{\mathcal{F}^{\mathrm{R}}(u^+_{j+1/2}) + \mathcal{F}^{\mathrm{R}}(u^-_{j+1/2,})}{2} - \frac{a_{j+1/2}(t)}{2}[u^+_{j+1/2}(t) - u^-_{j+1/2}(t)] \tag{A.18}$$

References

[1] P. Lax, Weak solutions of nonlinear hyperbolic equations and their numerical computation, Commun. Pure Appl. Math. 7 (1) (1954) 159–193.
[2] H. Nessyahu, E. Tadmor, Non-oscillatory central differencing for hyperbolic conservation laws, J. Comput. Phys. 87 (2) (1990) 408–463.
[3] F. Furtado, F. Pereira, S. Ribeiro, A new two-dimensional second order non-oscillatory central scheme applied to multiphase flows in heterogeneous porous media,(2008). arXiv preprint: 0803.4224
[4] A. Kurganov, E. Tadmor, New high-resolution central schemes for nonlinear conservation laws and convection–diffusion equations, J. Comput. Phys. 160 (1) (2000) 241–282.
[5] A. Kurganov, G. Petrova, A third-order semi-discrete genuinely multidimensional central scheme for hyperbolic conservation laws and related problems, Numer. Math. 88 (4) (2001) 683–729.
[6] A. Kurganov, G. Petrova, Central-upwind schemes on triangular grids for hyperbolic systems of conservation laws, Numer. Methods Partial Differ. Equ. 21 (3) (2005) 536–552.
[7] P. Arminjon, A. St-Cyr, A. Madrane, Non-oscillatory Lax–Friedrichs type central finite volume methods for 3-D flows on unstructured tetrahedral grids, in: Hyperbolic Problems: Theory, Numerics, Applications, in: International Series of Numerical Mathematics, vol. 140, 2001, pp. 59–68.
[8] A. Madrane, R. Vaillancourt, Three-dimensional adaptive central schemes on unstructured staggered grids, SIAM J. Sci.c Comput. 31 (5) (2009) 3979–3999.
[9] C. Greenshields, H. Weller, L. Gasparini, J. Reese, Implementation of semi-discrete, non-staggered central schemes in a colocated, polyhedral, finite volume framework, for high-speed viscous flows, Int. J. Numer. Methods Fluids 63 (1) (2010) 1–21.
[10] S. Karni, E. Kirr, A. Kurganov, G. Petrova, Compressible two-phase flows by central and upwind schemes, Math. Model. Numer. Anal. 38 (3) (2004) 477–493.
[11] S. Evje, T. Flåtten, Hybrid central-upwind schemes for numerical resolution of two-phase flows, ESAIM Math. Model. Numer. Anal. 39 (2) (2005) 253–273.
[12] D. Zeidan, The Riemann problem for a hyperbolic model of two-phase flow in conservative form, Int. J. Comput. Fluid Dyn. 25 (6) (2011) 299–318.
[13] D. Zeidan, A. Slaouti, Validation of hyperbolic model for two-phase flow in conservative form, Int. J. Comput. Fluid Dyn. 23 (9) (2009) 623–641.
[14] R. Kupferman, A numerical study of the axisymmetric Couette–Taylor problem using a fast high-resolution second-order central scheme, SIAM J. Sci.c Comput. 20 (3) (1998a) 858–877.
[15] R. Kupferman, Simulation of viscoelastic fluids: Couette–Taylor flow, J. Comput. Phys. 147 (1) (1998b) 22–59.
[16] R. Kupferman, M. Denn, Simulation of the evolution of concentrated shear layers in a Maxwell fluid with a fast high-resolution finite-difference scheme, J. Non-Newton. Fluid Mech. 84 (2) (1999) 275–287.
[17] R. Grauer, F. Spanier, A note on the use of central schemes for incompressible Navier–Stokes flows, J. Comput. Phys. 192 (2) (2003) 727–731.
[18] R. Kupferman, E. Tadmor, A fast, high resolution, second-order central scheme for incompressible flows, Proc. Natl. Acad. Sci. 94 (10) (1997) 4848–4852.
[19] E. Abreu, F. Pereira, S. Ribeiro, Central schemes for porous media flows, Comput. Appl. Math. 28 (1) (2009) 87–110.
[20] F. Pereira, A. Rahunanthan, A semi-discrete central scheme for the approximation of two-phase flows in three space dimensions, Math. Comput. Simul. 81 (10) (2011) 2296–2306.
[21] R. Issa, Solution of implicitly discretised fluid flow equations by operator splitting, J. Comput. Phys. 62 (1986) 40–65.
[22] H. Jasak, Error Analysis and Estimation for the Finite Volume Method with Applications to Fluid Flows, Department of Mechanical Engineering Imperial College of Science, Technology and Medicine, London, UK, 1996. (Ph.D. thesis).
[23] S. Márquez Damián, An Extended Mixture Model for the Simultaneous Treatment of Short and Long Scale Interfaces, FICH, Universidad Nacional del Litoral, Santa Fe, Argentina, 2013. (Ph.D. thesis).
[24] R. Bird, W. Stewart, E. Lightfoot, Transport Phenomena, Wiley, 2007.
[25] J. Ferziger, M. Peric, Computational Methods for Fluid Dynamics, vol. I, Springer-Verlag, 2002.
[26] A. Harten, High resolution schemes for hyperbolic conservation laws, J. Comput. Phys. 49 (3) (1983) 357–393.
[27] G.-S. Jiang, D. Levy, C.-T. Lin, S. Osher, E. Tadmor, High-resolution nonoscillatory central schemes with nonstaggered grids for hyperbolic conservation laws, SIAM J. Numer. Anal. 35 (6) (1998) 2147–2168.
[28] Y. Liu, C. Shu, E. Tadmor, M. Zhang, Non-oscillatory hierarchical reconstruction for central and finite volume schemes, Commun. Comput. Phys. 2 (2007) 933–963.
[29] P. Sweby, High resolution schemes using flux limiters for hyperbolic conservation laws, SIAM J. Numer. Anal. (1984) 995–1011.
[30] M. Darwish, F. Moukalled, TVD schemes for unstructured grids, Int. J. Heat Mass Transf. 46 (4) (2003) 599–611.
[31] Y. Liu, O. Hinrichsen, CFD modeling of bubbling fluidized beds using OpenFOAM®: Model validation and comparison of TVD differencing schemes, Comput. Chem. Eng. 69 (2014) 75–88.
[32] F. Denner, B. van Wachem, Compressive VOF method with skewness correction to capture sharp interfaces on arbitrary meshes, J. Comput. Phys. 279 (2014) 127–144.
[33] F. Denner, B. van Wachem, TVD differencing on three-dimensional unstructured meshes with monotonicity-preserving correction of mesh skewness, J. Comput. Phys. 298 (2015) 466–479.
[34] A.L. Zanotti, Modelado del Flujo Multifase en la Produccion de Acero por Colada Continua, Facultad de Ingeniería y Ciencas Hídricas, UNL, Santa Fe, Argentina, 2007. (Ph.D. thesis).
[35] D. Drew, S. Passman, Theory of Multicomponent Fluids, Springer Verlag, 1999.
[36] M. Ishii, T. Hibiki, Thermo-Fluid Dynamics of Two-Phase Flow, Springer Verlag, 2010.
[37] S. Márquez Damián, G. Buscaglia, Water/oil separation modeling by population balance equations-solution of the probability density function, Mec. Comput. XXXIII (2014) 453–472.

[38] C. Drumm, M. Attarakih, H. Bart, Coupling of CFD with DPBM for an RDC extractor, Chem. Eng. Sci. 64 (4) (2009) 721–732.
[39] M. Manninen, V. Taivassalo, S. Kallio, On the Mixture Model for Multiphase Flow, Technical Research Centre of Finland, 1996.
[40] L. Schiller, Z. Naumann, A drag coefficient correlation, Z. Ver. Deutsch. Ing. 77 (1935) 318.
[41] P. Bohorquez, Finite volume method for falling liquid films carrying monodisperse spheres in Newtonian regime, AIChE J. 58 (8) (2012) 2601–2616.
[42] S. Márquez Damián, N.M. Nigro, An extended mixture model for the simultaneous treatment of small-scale and large-scale interfaces, Int. J. Numer. Methods Fluids 75 (8) (2014) 547–574.
[43] H.G. Weller, G. Tabor, H. Jasak, C. Fureby, A tensorial approach to computational continuum mechanics using object-oriented techniques, Comput. Phys. 12 (6) (1998) 620–631.
[44] S. Márquez Damián, J. Giménez, N. Nigro, gdbOF: A debugging tool for OpenFOAM®, Adv. Eng. Softw. 47 (1) (2012) 17–23.
[45] B. van Leer, Towards the ultimate conservative difference scheme. V. A second-order sequel to Godunov's method, J. Comput. Phys. 32 (1) (1979) 101–136.
[46] H. Nessyahu, E. Tadmor, The convergence rate of approximate solutions for nonlinear scalar conservation laws, SIAM J. Numer. Anal. 29 (6) (1992) 1505–1519.
[47] R. LeVeque, Finite volume methods for hyperbolic problems, Cambridge Univ Press, 2002.
[48] M. Nigam, Numerical simulation of buoyant mixture flows, Int. J. Multiph. Flow 29 (6) (2003) 983–1015.
[49] A. Boycott, Sedimentation of blood corpuscles, Nature 104 (1920) 532.
[50] E. Ponder, On sedimentation and rouleaux formation-I, Exp. Physiol. 15 (3) (1925) 235–252.
[51] H. Nakamura, K. Kuroda, La cause de l'acceleration de la vitesse de sedimentation des suspensions dans les recipients inclines, Keijo J. Med. 8 (1937) 256–296.
[52] A. Acrivos, E. Herbolzheimer, Enhanced sedimentation in settling tanks with inclined walls, J. Fluid Mech. 92 (3) (1979) 435–457.
[53] E. Barnea, J. Mizrahi, A generalized approach to the fluid dynamics of particulate systems: Part 1. General correlation for fluidization and sedimentation in solid multiparticle systems, Chem. Eng. J. 5 (2) (1973) 171–189.
[54] R. Davis, E. Herbolzhiemer, A. Acrivos, The sedimentation of polydisperse suspensions in vessels having inclined walls, Int. J. Multiph. Flow 8 (6) (1982) 571–585.